

# Novel Optimal Trajectory Design in UAV-Assisted Networks: A Mechanical Equivalence-Based Strategy

Xiaopeng Yuan, Yulin Hu, Deshi Li and Anke Schmeink

## Abstract

Unmanned aerial vehicles (UAVs), also known as drones, have already been widely implemented in wireless networks for promoting network performance and enabling new services. To efficiently explore the diversity introduced by the mobility of UAV, many efforts have been made in the design of the UAV trajectory under various wireless scenarios. However, the continuity of a UAV trajectory in both time and topology forces researchers to approximate the UAV trajectory by a discrete model, which always results in a sub-optimal solution. To tackle the difficulty and obtain the optimal trajectory, in this work we introduce an artificial potential field (APF) to reformulate the objective in trajectory design, with which the UAV trajectory problem can be completely equivalent to a mechanical problem. In such mechanical problem, the UAV trajectory is represented by an extremely soft and thin rope with variable density carrying UAV speed information, and the original objective of optimizing the system performance is transformed to minimizing the overall artificial potential energy on the rope. As a result, the rope in the optimal solution stays in a state of equilibrium and the UAV trajectory can be equivalently optimized by designing the shape of a rope under the APF via mechanical principles. We provide a case study to describe in detail the problem equivalence, i.e., taking a single-user network as an example in which the throughput between UAV and the user is considered as the objective performance. In particular, the optimal trajectory of a UAV is constructed based on mechanical principles, while the global optimality is also rigorously proved and further confirmed via simulations. Moreover, we also highlight that the novel strategy of constructing equivalent mechanical problem has the possibilities to be extended to various UAV trajectory problems under different scenarios with different performance optimization objectives.

## Index Terms

UAV, trajectory design, artificial potential field (APF), mechanical equivalence, equilibrium state.

## I. INTRODUCTION

With their great flexibility, unmanned aerial vehicles (UAVs) have enabled enormous potential deployments in various domains, like cargo transport, environment monitoring, rescue assistance

X. Yuan and Y. Hu are with School of Electronic Information, Wuhan University, 430072 Wuhan, China and ISEK Research Area, RWTH Aachen University, D-52074 Aachen, Germany. (Email:yuan@isek.rwth-aachen.de, yulin.hu@ieee.org). Y. Hu is the corresponding author. Deshi Li is with School of Electronic Information, Wuhan University, 430072 Wuhan, China, (Email: dsli@whu.edu.cn). A. Schmeink is with ISEK Research Area/Lab, RWTH Aachen University, D-52074 Aachen, Germany. (Email: schmeink@isek.rwth-aachen.de).

and mineral exploration [1]–[3]. Especially in wireless networks, the high mobility of UAVs helps to avoid the possible blockage in wireless signal transportation [4], [5] and to construct wireless channels with much higher quality, in comparison to those in traditional static networks [6]. To exploit these advantages, the static deployment position of UAVs has been carefully designed to raise the network performance, e.g., to enlarge the coverage for ground users while deploying UAVs as a base station [7]–[9] and to enhance the reliability of wireless connection while applying UAVs as a relay [10]. Moreover, also for wireless networks where UAVs have taken over communication tasks, the trajectory of a mobile UAV is optimized (predesigned before starting the tasks) aiming at maximizing the channel capacity [11]–[13], improving energy efficiency [14]–[17], and minimizing the total task completion time [18]. However, for such UAV trajectory (pre)design, a huge difficulty is that the trajectory is generally required to be continuous in both time and (the coordinates of the UAVs) location, i.e., an infinite number of variables needs to be optimized at the same time.

To deal with this difficulty, the most popular strategy in the literature is to approximate the continuous trajectory with a large number of discrete points while each two neighbour points are constrained by a maximum distance [13]–[18]. The trajectory is then **approximately** optimized by designing the positions of these discrete points. The obvious drawbacks of this strategy are: i. the resulted trajectory solution is sub-optimal, and ii. the accuracy of the approximation is an issue, while improving the accuracy significantly increases the complexity of the strategy. On the other hand, as another trajectory design strategy, a successive-hover-fly (SHF) structure is inserted in UAV trajectory [11], [12], [19], where the UAV is assumed to have hovering and flying behaviours, i.e., it successively hovers at different hovering points with different hovering durations. Following the SHF structure, the trajectory is designed via determining the positions of these hovering points and corresponding hovering durations. Nevertheless, this strategy only works for scenarios where the SHF structure assumption of the UAV trajectory does not lose the optimality of the original objective of the design. In addition, although the complexity of the SHF-based trajectory design is significantly reduced in comparison to the popular approximation strategy, its optimality/accuracy is indeed sacrificed. This is due to the fact that the UAV is assumed to fly between hovering points along straight lines in an SHF structure. Hence, the optimality only holds for a one-dimensional (1D) special topology [19] and is definitely inaccurate for general scenarios where the UAV possibly flies via an arc/curve trajectory. To the best of our knowledge, the global optimal UAV trajectory has not been obtained or mathematically described in application scenarios with a general topology.

In this paper, we introduce a mechanical concept, namely the artificial potential field (APF), to

the UAV trajectory design for a general UAV-enabled network with a general network topology. A completely novel strategy is proposed, in which we first represent the design objective and the UAV trajectory respectively by the APF and a physical rope with certain density carrying the information of the UAV speed. As a result, the UAV trajectory design problem is equivalently transformed to a mechanical problem minimizing the overall potential energy on the equivalent rope. Due to the fact that the rope must stay in a state of equilibrium when the overall potential energy is minimized [20], the UAV trajectory is optimally constructed by designing the rope shape based on the mechanical principles in equilibrium. In the following sections, the design strategy is first illustrated via a single-user example network, in which the throughput between UAV and user is considered as objective to be maximized. Then the global optimal trajectory is mathematically constructed. After that, we confirm the optimality of our proposed strategy in single-user network through simulations and highlight the abundant possible extensions of the novel strategy in UAV trajectory designs. The contributions of this paper are listed as follows:

- **Physical Equivalence of Trajectory Design:** In this work, we have proposed a novel strategy for UAV trajectory design. For the first time, the UAV trajectory design problem is completely equivalent to a physical problem with the assistance of APF. With the physical equivalence, the UAV trajectory design problem becomes analyzable and the optimal solution can be characterized via physical principles. The physical equivalence will definitely facilitate the analysis and characterization of various trajectory design problem.
- **Optimal Trajectory Solution for Single-User Network:** To clarify the novel strategy, we start with a single-user network. While targeting at maximizing the overall throughput between UAV and the user, we characterize the UAV speed in optimal solution and based on physical principles optimally constructed the optimal trajectory for UAV. Since most of the existing strategies for UAV trajectory design can only guarantee a suboptimal solution, our work with optimality has shown significant analytical contributions. Furthermore, the optimality has also shown to be able to be extended in single-user network with many complex models and objectives.
- **Closed-Form Trajectory Solution:** Beside of the optimality, for the first time, we also characterize the closed-form expression for the continuous optimal UAV trajectory. With the closed-form expression, the computational complexity for constructing the optimal trajectory is extremely lower. The extremely high efficiency will be much attractive in some latency-critical scenarios.

It should be mentioned and clarified that the concept of APF has been proposed in robot path design [21] and then extended to some UAV path designs [22]. However, in these studies, the APF has only applied as an approximation tool for the algorithms to approximately model the obstacles constraints, i.e., avoiding collisions on the path (not a trajectory containing the location and speed information at each time point), which does not introduce any mechanical significance on the APF. This is totally different from our proposed strategy which equivalently totally transforms the trajectory problem formulation to a mechanical one and obtains the optimal trajectory solution.

The rest of this paper is organized as follows. In Section II, we describe our considered example single-user network and formulate a UAV trajectory design problem aiming at maximizing the overall throughput. Next, the original problem is reformulated and completely equivalent to a mechanical problem in Section III. Then, we equivalently focus on the mechanical problem and construct the optimal solution for UAV trajectory in Section IV, which requires a design of an optimal initial tension. In Section V, we provided an approach for obtaining the optimal initial tension. Finally, the work is validated via simulations in Section VI and concluded in Section VII.

## II. PROBLEM STATEMENT IN SINGLE-USER NETWORK

To present this novel UAV trajectory design strategy, we consider a single-user network as an example, where a UAV is deployed as a mobile base station as shown in Fig. 1(a). The user is placed at position  $\mathbf{D}_0 = (w_{0,x}, w_{0,y})$  on the ground. The UAV is operated at a fixed altitude  $H > 0$  being responsible for wirelessly communicating with the ground user (GU). The horizontal position of the UAV at time point  $t \geq 0$  is represented by  $(x(t), y(t))$ , which is clearly a continuous function in time  $t$ . Moreover, the UAV is assumed to have a maximum speed limit  $V$ , i.e.,  $\|(\dot{x}(t), \dot{y}(t))\|_2 \leq V$ ,  $\forall t \geq 0$ . Further note that we consider a rotary-wing UAV. Since the flying speed of rotary-wing UAV can be generally adjusted in a very short time [14], [15], we assume the acceleration limit for UAV is ignored. We denote by  $T$  the communication time duration between the UAV and the GU, e.g., the duration could be allocated by a higher layer scheduler. Then, for any time point  $t$  on the interested UAV trajectory, we have  $t \in [0, T]$ . In particular, within this duration of  $T$ , the UAV is required to fly from a given starting point  $\mathbf{D}_1 = (w_{1,x}, w_{1,y})$  to the given destination  $\mathbf{D}_2 = (w_{2,x}, w_{2,y})$ , as implied in Fig. 1(a), which implies that

$$(x(0), y(0)) = \mathbf{D}_1 = (w_{1,x}, w_{1,y}), \quad (x(T), y(T)) = \mathbf{D}_2 = (w_{2,x}, w_{2,y}). \quad (1)$$

We consider the scenario where  $\|\mathbf{D}_1 - \mathbf{D}_2\|_2 = \sqrt{(w_{1,x} - w_{2,x})^2 + (w_{1,y} - w_{2,y})^2} \leq VT$  holds, otherwise the UAV is not capable of completing the flight from  $\mathbf{D}_1$  to  $\mathbf{D}_2$  within allocated time duration  $T$ , i.e., the trajectory design is infeasible. Note that it is reasonable to assume given starting

and ending points for UAV trajectory design, since the UAV is generally responsible for multi-tasks in practice and for a certain task the starting and ending points highly rely on the previous and next UAV tasks.

We refer to the channel gain to represent the channel quality. We adopt to apply the free-space path loss model as in [23]–[25] due to the high probability of line-of-sight (LoS) between UAV and GU in short range [6]. The channel gain at time  $t$  is given by  $h(x(t), y(t)) = \frac{\beta}{r(x(t), y(t))^2 + H^2}$ , where  $\beta$  denotes the channel gain at a reference distant of  $1m$  and  $r(x(t), y(t))$  represents the horizontal distance from point  $(x(t), y(t))$  to the GU at position  $\mathbf{D}_0$ , i.e.,

$$r(x(t), y(t)) = \sqrt{(x(t) - w_{0,x})^2 + (y(t) - w_{0,y})^2}. \quad (2)$$

For the wireless communication between the UAV and the GU, we denote by  $P$  the transmit power from the GU in the uplink scenario (or from the UAV in the downlink case). Therefore, the maximum transmission rate between the GU and the UAV at time  $t$  is formulated as

$$R(x(t), y(t)) = B \log_2 \left( 1 + \frac{P}{\sigma^2} \frac{\beta}{r(x(t), y(t))^2 + H^2} \right), \quad (3)$$

where  $B$  represents the bandwidth and  $\sigma^2$  is the noise power level. As a result, the corresponding total throughput over time duration  $T$  is given by

$$U(\{x(t), y(t)\}) = \int_0^T R(x(t), y(t)) dt. \quad (4)$$

Following the above system model, we aim at maximizing the throughput  $U(\{x(t), y(t)\})$  by optimizing the UAV trajectory  $\{x(t), y(t)\}$  under the maximum UAV speed limit  $V$ . Thus, the original problem is described as

$$(\text{OP}) : \max_{\{x(t), y(t)\}} U(\{x(t), y(t)\}) \quad (5a)$$

$$s.t. \quad \|(\dot{x}(t), \dot{y}(t))\|_2 \leq V, \quad \forall t \in [0, T], \quad (5b)$$

$$(x(0), y(0)) = (w_{1,x}, w_{1,y}), \quad (5c)$$

$$(x(T), y(T)) = (w_{2,x}, w_{2,y}). \quad (5d)$$

Clearly, this original problem (OP) contains an infinite number of variables  $(x(t), y(t))$ , as there are an infinite number of time points  $t$  in the trajectory  $\{x(t), y(t)\}$ . Moreover, the UAV trajectory is continuous in both time and (the coordinates of the UAV's) location, which makes the trajectory design quite challenging. In addition, the objective function is apparently non-convex, which implies that an efficient optimal solution is impossible to be obtained through convex optimization technology.

To construct the optimal UAV trajectory, in the next section we introduce an equivalent mechanical

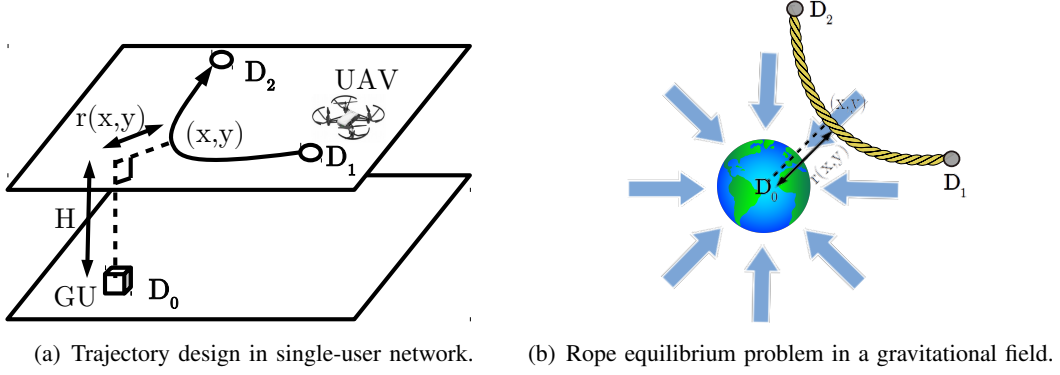


Fig. 1. Examples of two kinds of problems.

problem for problem (OP) including a set of corresponding equivalent mechanical conceptions.

### III. PROBLEM EQUIVALENCE IN MECHANICS

In this section, we first reformulate problem (OP), and subsequently construct a mechanical problem with exactly the same form. By introducing the concept of artificial potential energy into the trajectory design, we further show that problem (OP) can be solved by equivalently solving a mechanical problem.

#### A. Reformulation of Problem (OP)

Let us consider a different way of representing a UAV trajectory. Note that at each time point the UAV trajectory information can be actually fully determined if the UAV location (with moving direction) and speed are given. Hence, the whole trajectory can be described by two groups of information, namely path information and speed information. In particular, for any UAV trajectory  $\{x(t), y(t)\}$ , the corresponding UAV path  $\{\hat{x}(s), \hat{y}(s)\}$  can be defined as

$$(\hat{x}(s), \hat{y}(s)) = (x(t), y(t)), \text{ while } \int_0^t \|(\dot{x}(\tau), \dot{y}(\tau))\|_2 d\tau = s. \quad (6)$$

The path variable  $s$  denotes the path length from the given starting point  $D_1$  to  $(\hat{x}(s), \hat{y}(s))$  along the trajectory  $\{x(t), y(t)\}$ . Clearly, we have  $s \in [0, S]$ , where  $S = \int_0^T \|(\dot{x}(\tau), \dot{y}(\tau))\|_2 d\tau$  is the total path length of trajectory  $\{x(t), y(t)\}$ . Hence, the path  $\{\hat{x}(s), \hat{y}(s)\}$  also starts from point  $D_1$  and ends at point  $D_2$ , so that  $(\hat{x}(0), \hat{y}(0)) = D_1$  and  $(\hat{x}(S), \hat{y}(S)) = D_2$ .

On the other hand, the speed information can be expressed based on the path model. In particular, for any given path variable  $s$ , there is a unique corresponding UAV speed  $v(s)$ , which is given by

$$v(s) = \|(\dot{x}(\tau), \dot{y}(\tau))\|_2, \text{ while } \int_0^t \|(\dot{x}(\tau), \dot{y}(\tau))\|_2 d\tau = s. \quad (7)$$

Hence, (8) holds, which ensures that the UAV finishes the flight within (allocated) time duration  $T$ .

$$\int_0^S \frac{ds}{v(s)} = T \quad (8)$$

If there are hovering behaviours in the trajectory, where the UAV speed is zero, the above reformulation as well as (8) with term  $\frac{1}{v(s)}$  also hold after introducing a Dirac delta function. For instance, when the UAV has a hovering behaviour at point  $(\hat{x}(s_0), \hat{y}(s_0))$  with hovering duration  $\Delta t > 0$ , the corresponding UAV speed  $v(s_0)$  becomes zero and can be expressed as

$$v(s_0) = \frac{1}{\Delta t} \cdot \frac{1}{\delta(0)}, \quad (9)$$

where  $\delta(0)$  is the Dirac delta function. Note that as  $\delta(0)$  is indeed infinity, the actual UAV speed  $v(s_0)$  is still zero, which conforms to the hovering behaviour. However, it holds that

$$\int_{s_{0-}}^{s_{0+}} \frac{1}{v(s)} ds = \Delta t. \quad (10)$$

Following the path and speed information models, the overall throughput is then described by

$$\hat{U}(\{\hat{x}(s), \hat{y}(s)\}, v(s)) = \int_0^S R(\hat{x}(s), \hat{y}(s)) \frac{1}{v(s)} ds. \quad (11)$$

While substituting the trajectory variable  $\{x(t), y(t)\}$  in problem (OP) with the variable of the path  $\{\hat{x}(s), \hat{y}(s)\}$  and speed  $v(s)$ , problem (OP) can be equivalently reformulated as

$$(P1) : \max_{\{\hat{x}(s), \hat{y}(s)\}, v(s), S} \int_0^S R(\hat{x}(s), \hat{y}(s)) \frac{1}{v(s)} ds \quad (12a)$$

$$s.t. \quad \frac{1}{v(s)} \geq \frac{1}{V}, \quad \forall s \in [0, S], \quad (12b)$$

$$\int_0^S \frac{1}{v(s)} ds = T, \quad (12c)$$

$$(\hat{x}(0), \hat{y}(0)) = (w_{1,x}, w_{1,y}), \quad (12d)$$

$$(\hat{x}(S), \hat{y}(S)) = (w_{2,x}, w_{2,y}). \quad (12e)$$

Note that as implied in (10), although the value of  $\frac{1}{v(s)}$  may be infinite, the integral  $\int_0^S \frac{1}{v(s)} ds$  is bounded by  $T$  as shown in constraint (12c). The reformulated problem (P1) requires a joint optimization of path variable  $\{\hat{x}(s), \hat{y}(s)\}$ , speed  $v(s)$  and a total path length  $S$ , which is apparently still strenuous to be addressed via typical optimization methods.

### B. Variable-Density Rope Equilibrium Problem

Now, let us consider a mechanical problem in a space with a single force field. A mass point, being with mass of  $M$ , is located at fixed position  $\mathbf{D}_0 = (w_{0,x}, w_{0,y})$ , i.e., the earth in Fig. 1(b). The gravitational potential generated by the mass point at any other position  $(\hat{x}', \hat{y}')$  is given by

$$R'(\hat{x}', \hat{y}') = -\frac{GM}{r(\hat{x}', \hat{y}')}, \quad (13)$$

where  $G$  is the gravitational constant, and  $r(\hat{x}', \hat{y}')$  denotes the distance from point  $(\hat{x}', \hat{y}')$  to  $\mathbf{D}_0$  as defined in (2). In addition, a variable-density rope with mass of  $m$  is also placed in the space shown in Fig. 1(b). The two ends of the rope are fixed at positions  $\mathbf{D}_1 = (w_{1,x}, w_{1,y})$  and  $\mathbf{D}_2 = (w_{2,x}, w_{2,y})$ , respectively. We assume that the rope is thin enough such that can be considered as a single line. We denote by a continuous functions  $\{\hat{x}'(s), \hat{y}'(s)\}$  the shape of the rope, where the variable  $s \in [0, S']$  represents the partial rope length from  $\mathbf{D}_1$  to the point  $(\hat{x}'(s), \hat{y}'(s))$ . In addition,  $S'$  represents the total rope length, which is also a variable as the line density of the rope is changeable. Moreover, the line density  $\rho(s)$  of the rope is lower-bounded by a minimum  $\rho_{\min} > 0$  (which guarantees the existence of the rope, i.e.,  $\sqrt{(w_{1,x} - w_{2,x})^2 + (w_{1,y} - w_{2,y})^2} \cdot \rho_{\min} \leq m$ ). We further assume the rope to be sufficiently soft, so that each rope segment can be concentrated on a single point. For instance, with a given partial length  $s_0 \in [0, S']$ , if a mass point is formed at position  $(\hat{x}'(s_0), \hat{y}'(s_0))$  with mass  $m_0$ , the corresponding line density is  $\rho(s_0) = m_0 \delta(0)$  with an infinite value. Although the rope density is not upper-bounded, the definite integration over it (from 0 to the given  $S'$ ) representing the weight of the corresponding rope segment is actually a constant, which is given by

$$\int_0^{S'} \rho(s) ds = m. \quad (14)$$

As a result, the total gravitation potential energy of the rope is then given by

$$\hat{U}'(\{\hat{x}'(s), \hat{y}'(s)\}, \rho(s)) = \int_0^{S'} R'(\hat{x}'(s), \hat{y}'(s)) \rho(s) ds. \quad (15)$$

Therefore, to study the static rope appearance, a problem minimizing the total potential energy through jointly optimizing the rope shape  $\{\hat{x}'(s), \hat{y}'(s)\}$ , rope density  $\rho(s)$  and the total rope length  $S'$ , can be established as

$$(P2) : \min_{\{\hat{x}'(s), \hat{y}'(s)\}, \rho(s), S'} \int_0^{S'} R'(\hat{x}'(s), \hat{y}'(s)) \rho(s) ds \quad (16a)$$

$$s.t. \quad \rho(s) \geq \rho_{\min}, \quad \forall s \in [0, S'], \quad (16b)$$

$$\int_0^{S'} \rho(s) ds = m, \quad (16c)$$

$$(\hat{x}'(0), \hat{y}'(0)) = (w_{1,x}, w_{1,y}), \quad (16d)$$

$$(\hat{x}'(S'), \hat{y}'(S')) = (w_{2,x}, w_{2,y}). \quad (16e)$$

According to the *minimum total potential energy principle* [20], if the rope has minimized the total potential energy  $U'(\{\hat{x}'(s), \hat{y}'(s)\})$ , i.e., being the optimal solution to (P2), it must already be in a state of equilibrium (with zero net force and zero net torque). Otherwise, with effects of nonzero net force or nonzero net torque, a better solution with lower potential energy will be found. Following



UAV Trajectory Design	$\Rightarrow$	Equivalent Mechanical Problem
UAV trajectory	$\Rightarrow$	density-variable rope
UAV path $\{\hat{x}(s), \hat{y}(s)\}$	$\Rightarrow$	rope shape $\{\hat{x}'(s), \hat{y}'(s)\}$
UAV path length $S$	$\Rightarrow$	rope length $S'$
UAV speed $v(s)$	$\Rightarrow$	reciprocal of rope line density $\frac{1}{\rho(s)}$
UAV speed limit $V$	$\Rightarrow$	reciprocal of minimum line density $\frac{1}{\rho_{\min}}$
allocated time duration $T$	$\Rightarrow$	rope mass $m$
maximum transmission rate $R(x, y)$	$\Rightarrow$	opposite of artificial potential field $-R''(x, y)$
overall throughput $\hat{U}(\{\hat{x}(s), \hat{y}(s)\}, v(s))$	$\Rightarrow$	opposite of artificial potential energy $-\hat{U}'(\{\hat{x}'(s), \hat{y}'(s)\}, \rho(s))$

Fig. 2. Table for problem equivalence.

the mechanical rules in equilibrium [26], we can quickly obtain the optimal solution to (P2).

### C. Problem Equivalence

By carefully comparing and examining problems (P1) and (P2), we can find a set of equivalences between them, with which the trajectory design problem (P1) can be equivalent to a mechanical problem. More specifically, the UAV path  $\{\hat{x}(s), \hat{y}(s)\}$ , total path length  $S$  and UAV speed  $v(s)$  can be equivalent to the rope shape  $\{\hat{x}'(s), \hat{y}'(s)\}$ , total rope length  $S'$  and the reciprocal of rope line density  $\frac{1}{\rho(s)}$ , respectively, as shown in Fig. 2. Moreover, the speed limit  $V$  and the total allocated time  $T$  equivalent respectively to the reciprocal of minimum line density  $\frac{1}{\rho_{\min}}$  and the total rope mass  $m$ . Accordingly, the maximum transmission rate  $R(\hat{x}(s), \hat{y}(s))$  and the overall throughput  $\hat{U}(\{\hat{x}(s), \hat{y}(s)\}, v(s))$  are corresponding to the opposite of gravitational potential  $-R'(\hat{x}'(s), \hat{y}'(s))$  and the opposite of total gravitation potential energy  $-\hat{U}'(\{\hat{x}'(s), \hat{y}'(s)\}, \rho(s))$ , respectively. On the other hand, different from these variable equivalences, the objectives of the two problems, i.e., the maximum transmission rate  $R(\hat{x}(s), \hat{y}(s))$  and the gravitational potential  $R'(\hat{x}'(s), \hat{y}'(s))$ , have completely different expressions, as shown in (3) and (13). Thus, problems (P1) and (P2) are not equivalent, i.e., the objective of problem (P2) needs to be further reformulated.

Fortunately, as problem (P2) is constructed in a gravitational potential field  $R'(x, y)$ , the maximum transmission rate in (3) can be also presented via defining another artificial potential field  $R''(x, y)$  in the following way: for any given position  $(x, y)$ ,

$$R''(x, y) = -R(x, y) = -B \log_2 \left( 1 + \frac{P}{\sigma^2} \frac{\beta}{r(x, y)^2 + H^2} \right), \quad (17)$$

which results in the same objective expression as the one of problem (P1). Hence, problem (P1) is equivalent to a variable-density rope equilibrium problem (P3) in the artificial potential field (APF) given as follows

$$(P3) : \min_{\{\hat{x}'(s), \hat{y}'(s)\}, \rho(s), S'} \hat{U}''(\{\hat{x}'(s), \hat{y}'(s)\}, \rho(s)) = \int_0^{S'} R''(\hat{x}'(s), \hat{y}'(s)) \rho(s) ds \quad (18a)$$

$$s.t. \quad (16b), (16c), (16d), (16e).$$

So far, the original trajectory design problem has been equivalently transformed to a mechanical problem, as described in Fig. 2. This motivates us to first rigorously solve the rope equilibrium problem (P3) in the APF (17) by applying mechanical principles. Equivalently, the optimal trajectory for problem (OP) can be subsequently constructed from the optimal solution to problem (P3).

#### IV. OPTIMAL TRAJECTORY CONSTRUCTION

To optimally solve problem (P3), in this section we first characterize the properties of the defined APF and then implement mechanical principles to construct the optimal solution. In particular, different construction strategies will be presented according to different total rope masses  $m$ , i.e., equivalently different allocated time duration  $T$  in the trajectory design problem.

##### A. APF Characterization

As a mechanical concept, a potential field has a corresponding force field, which is a vector field and described by the negative gradient of a scalar potential function. In the considered problem (P3), the generated force field of the proposed APF  $R''(x, y)$  is given by

$$\mathbf{g}(x, y) = -\nabla R''(x, y) = -\frac{dR''(x, y)}{dr(x, y)} \begin{pmatrix} \frac{\partial r(x, y)}{\partial x} \\ \frac{\partial r(x, y)}{\partial y} \end{pmatrix}. \quad (19)$$

Further note that it can be easily proved that the APF  $R''(x, y)$  in (17) has a monotonic property 1.

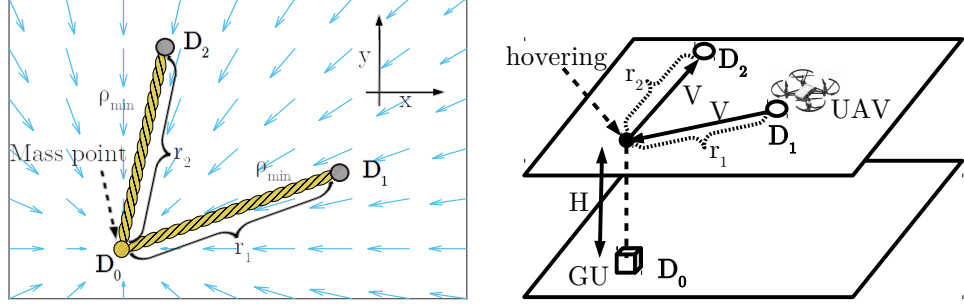
**Property 1.** *The APF  $R''(x, y)$  in (17) is a strictly monotonically increasing function in  $r(x, y)$ , when  $r(x, y) \geq 0$ .*

Hence, we have  $\frac{dR''(x, y)}{dr(x, y)} > 0$  when  $r(x, y) > 0$ . As  $r(x, y)$  denotes the distance from  $(x, y)$  to  $\mathbf{D}_0$ , the force field  $\mathbf{g}(x, y)$  is actually a vector towards a centre point  $\mathbf{D}_0$  with an absolute value of

$$|\mathbf{g}(x, y)| = \frac{dR''(x, y)}{dr(x, y)} = \frac{2\beta BP}{\sigma^2 \ln 2} \frac{r(x, y)}{r(x, y)^2 + H^2} \frac{1}{r(x, y)^2 + H^2 + \frac{\beta P}{\sigma^2}}. \quad (20)$$

This implies that the force field  $\mathbf{g}(x, y)$  is a centralized vector field with the centre at  $\mathbf{D}_0$ . An example force field can be observed in Fig. 3(a). In addition, the force field becomes zero only when  $(x, y)$  is the same point as  $\mathbf{D}_0$ , i.e.,  $r(x, y) = 0$ .

Same as the general force field, when a mass point is placed in the force field, a force will act on the mass point. Similarly, when this force has done some work, the work will be equal to the reduction of the artificial potential energy on the mass point. This again indicates that for the optimal rope shape in problem (P3), which is corresponding to the optimal trajectory of problem



(a) Optimal rope solution under APF with sufficient rope mass  $m \geq \rho_{\min}(r_1 + r_2)$ . (b) Equivalent optimal UAV trajectory with sufficient allocated time  $T \geq \frac{1}{v}(r_1 + r_2)$ .

Fig. 3. Optimal solution equivalence with sufficient rope mass  $m \geq \rho_{\min}(r_1 + r_2)$ .

(P1), the overall force on it cannot do any more positive work. Otherwise, a rope shape with lower artificial potential energy, namely a trajectory with higher throughput, will be found.

### B. Optimal Solution with Sufficient Rope Mass

We first consider a case where the total rope mass  $m$  is sufficiently large. Due to the assumptions of density variability and minimum line density constraint on the rope, a sufficiently large  $m$  signifies that the rope has the potential to be sufficiently long, since the maximum rope length is limited by  $\frac{m}{\rho_{\min}}$ . Furthermore, a monotonically increasing property of APF (17) has already been shown in Property 1. This indicates that a rope segment closer to point  $D_0$  results in a lower potential energy. Thus, with sufficiently large rope mass, the optimal rope solution should approach to the centre of APF as close as possible. In other words, in the optimal rope solution, the rope traverses along straight lines with the minimum line density of  $\rho_{\min}$  from point  $D_1$  to  $D_0$  then to  $D_2$  and the remaining mass forms a mass point at  $D_0$ , as displayed in Fig. 3(a). Mathematically, the solution can be formulated as

$$S'^* = r_1 + r_2, \quad (21)$$

$$(\hat{x}'^*(s), \hat{y}'^*(s)) = \begin{cases} \left( \frac{s(w_{0,x} - w_{1,x})}{r_1} + w_{1,x}, \frac{s(w_{0,y} - w_{1,y})}{r_1} + w_{1,y} \right), & s \in [0, r_1], \\ \left( \frac{(s-r_1)(w_{2,x} - w_{0,x})}{r_2} + w_{0,x}, \frac{(s-r_1)(w_{2,y} - w_{0,y})}{r_2} + w_{0,y} \right), & s \in (r_1, S'^*], \end{cases} \quad (22)$$

$$\rho^*(s) = \begin{cases} (m - \rho_{\min}(r_1 + r_2))\delta(0), & s = r_1, \\ \rho_{\min}, & s \neq r_1, \end{cases} \quad (23)$$

where  $r_1 = r(w_{1,x}, w_{1,y})$  and  $r_2 = r(w_{2,x}, w_{2,y})$  respectively denote the distances from two ends of rope, namely  $D_1$  and  $D_2$ , to the center  $D_0$  of APF. The solution is feasible only when  $m \geq \rho_{\min}(r_1 + r_2)$ . On the other hand, we can also mathematically prove the optimality of the constructed solution, when  $m \geq \rho_{\min}(r_1 + r_2)$ , as stated in Lemma 1.

**Lemma 1.** When  $m \geq \rho_{\min}(r_1 + r_2)$ , the rope defined by (21), (22) and (23) is the optimal solution of problem (P3).

*Proof.* The proof is provided in Appendix A.  $\square$

Equivalently, based on the optimal solution to problem (P3) defined by (21), (22) and (23), we can further obtain the optimal trajectory of problem (OP) in the case of  $T \geq \frac{1}{V}(r_1 + r_2)$ . It is depicted as in Fig. 3(b) with a hovering behaviour above the GU, and can be mathematically formulated as

$$(x^*(t), y^*(t)) = \begin{cases} \left( \frac{Vt(w_{0,x} - w_{1,x})}{r_1} + w_{1,x}, \frac{Vt(w_{0,y} - w_{1,y})}{r_1} + w_{1,y} \right), & t \in [0, \frac{r_1}{V}], \\ (w_{0,x}, w_{0,y}), & t \in (\frac{r_1}{V}, T - \frac{r_2}{V}], \\ \left( \frac{(Vt-T)(w_{2,x} - w_{0,x})}{r_2} + w_{2,x}, \frac{(Vt-T)(w_{2,y} - w_{0,y})}{r_2} + w_{2,y} \right), & t \in (T - \frac{r_2}{V}, T]. \end{cases} \quad (24)$$

### C. Optimal Solution with Insufficient Rope Mass

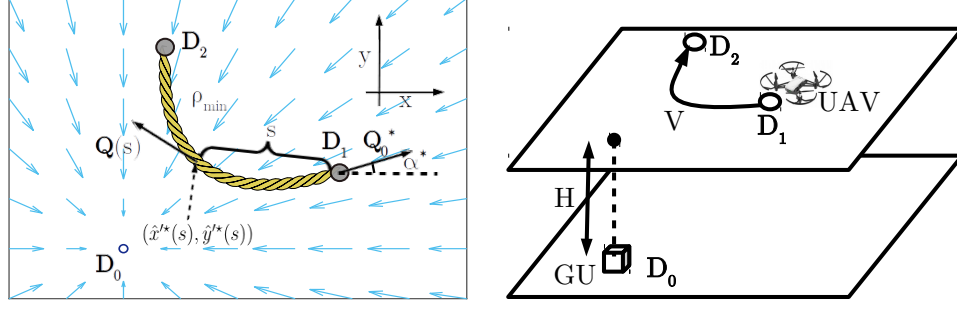
When  $m < \rho_{\min}(r_1 + r_2)$ , the maximum rope length  $\frac{m}{\rho_{\min}}$  is not enough to support the rope passing the centre  $\mathbf{D}_0$  of APF. Hence, for any sufficiently small rope segment in the corresponding optimal rope solution, there is a non-zero force generated from APF acting on it. As a result, to minimize the total artificial potential energy, each sufficiently small rope segment in the optimal rope (solution) has extended itself towards the centre  $\mathbf{D}_0$  as far as possible. In other words, the optimal rope (solution) should have a constant line density  $\rho_{\min}$ , i.e., the optimal line density  $\rho^*(s) = \rho_{\min}$ , and accordingly an optimal total rope length  $S'^* = \frac{m}{\rho_{\min}}$ . Otherwise, by extending part of the rope towards  $\mathbf{D}_0$ , a better solution can be constructed. More rigorously, we have the statement in Lemma 2.

**Lemma 2.** In the optimal rope solution  $\{\hat{x}'^*(s), \hat{y}'^*(s)\}$ ,  $\rho^*(s)$  and  $S'^*$  of problem (P3),  $\forall s_0 \in [0, S'^*]$ ,  $\rho^*(s_0) = \rho_{\min}$  holds, when  $(\hat{x}'^*(s_0), \hat{y}'^*(s_0)) \neq \mathbf{D}_0 = (w_{0,x}, w_{0,y})$ .

*Proof.* The proof is provided in Appendix B.  $\square$

When the rope mass is insufficient, the center point  $\mathbf{D}_0$  will be unavailable for the rope. According to the Lemma 2, the optimal rope solution of (P3) should always have the minimum line density, i.e.,  $\rho^*(s) = \rho_{\min}$ , with insufficient rope mass. Thus, the remaining difficulty becomes to be the design of optimal rope shape  $\{\hat{x}'^*(s), \hat{y}'^*(s)\}$ .

Now let us assume that in the optimal solution  $\{\hat{x}'^*(s), \hat{y}'^*(s)\}$ , the initial rope tension at point  $\mathbf{D}_1$  is given by  $\mathbf{Q}_0^*$  and has an angle  $\alpha^*$  to the positive  $x$ -axis, as shown in Fig. 4(a). Then, we further denote by  $\mathbf{Q}(s)$  the rope tension at point  $(\hat{x}'^*(s), \hat{y}'^*(s))$ . Note that in the optimal rope shape, the forces acting on the segment from  $\mathbf{D}_1$  to  $(\hat{x}'^*(s), \hat{y}'^*(s))$  must be balanced to guarantee



(a) Optimal rope solution under APF with insufficient rope mass  $m < \rho_{\min}(r_1 + r_2)$ . (b) Equivalent optimal UAV trajectory with insufficient allocated time  $T < \frac{1}{v}(r_1 + r_2)$ .

Fig. 4. Optimal solution equivalence with insufficient rope mass  $m < \rho_{\min}(r_1 + r_2)$ .

the rope in the state of equilibrium. Thus, the net forces in the directions of  $x$ -axis and  $y$ -axis are both zero, namely

$$\underbrace{|\mathbf{Q}_0^*| \cos \alpha^* + \int_0^s |\mathbf{g}(\hat{x}^{t*}(s_0), \hat{y}^{t*}(s_0))| \rho_{\min} \frac{w_{0,x} - \hat{x}^{t*}(s_0)}{r(\hat{x}^{t*}(s_0), \hat{y}^{t*}(s_0))} ds_0}_{A_1^*(s)} + |\mathbf{Q}(s)| \frac{d\hat{x}^{t*}(s)}{ds} = 0, \quad (25)$$

$$\underbrace{|\mathbf{Q}_0^*| \sin \alpha^* + \int_0^s |\mathbf{g}(\hat{x}^{t*}(s_0), \hat{y}^{t*}(s_0))| \rho_{\min} \frac{w_{0,y} - \hat{y}^{t*}(s_0)}{r(\hat{x}^{t*}(s_0), \hat{y}^{t*}(s_0))} ds_0}_{A_2^*(s)} + |\mathbf{Q}(s)| \frac{d\hat{y}^{t*}(s)}{ds} = 0. \quad (26)$$

Combining (25) with (26), we have

$$\frac{d\hat{y}^{t*}(s)}{d\hat{x}^{t*}(s)} = \frac{A_2^*(s)}{A_1^*(s)}. \quad (27)$$

Moreover, from the definition of segment length  $s$ , we have

$$\int_0^s \sqrt{1 + \left( \frac{d\hat{y}^{t*}(s_0)}{d\hat{x}^{t*}(s_0)} \right)^2} \frac{d\hat{x}^{t*}(s_0)}{ds_0} ds_0 = s. \quad (28)$$

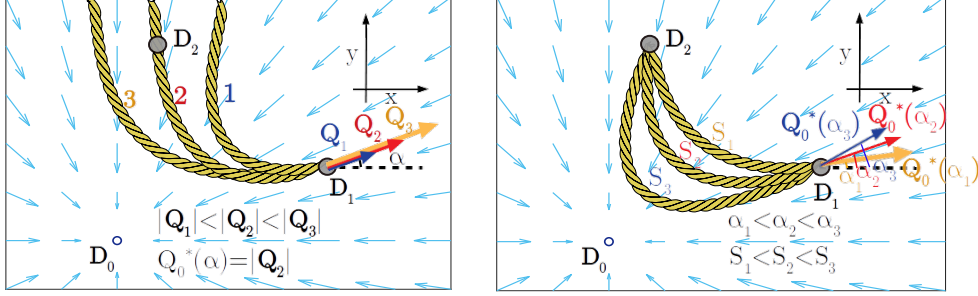
By taking derivative on both sides of (28) in  $s$ , we obtain the following relationship

$$\sqrt{\left( \frac{d\hat{x}^{t*}(s)}{ds} \right)^2 + \left( \frac{d\hat{y}^{t*}(s)}{ds} \right)^2} = 1. \quad (29)$$

Therefore, the first derivatives of the optimal rope shape  $\{\hat{x}^{t*}(s), \hat{y}^{t*}(s)\}$ , i.e.,  $\frac{d\hat{x}^{t*}(s)}{ds}$  and  $\frac{d\hat{y}^{t*}(s)}{ds}$ , can be uniquely obtained based on (25), (26), (27) and (29), which are more specifically given by

$$\frac{d\hat{x}^{t*}(s)}{ds} = \frac{-A_1^*(s)}{\sqrt{A_1^*(s)^2 + A_2^*(s)^2}}, \quad \frac{d\hat{y}^{t*}(s)}{ds} = \frac{-A_2^*(s)}{\sqrt{A_1^*(s)^2 + A_2^*(s)^2}}. \quad (30)$$

So far, we have found that as long as the optimal rope tension  $\mathbf{Q}_0^*$  at  $\mathbf{D}_1$ , including  $|\mathbf{Q}_0^*|$  and  $\alpha^*$ , is known, the optimal rope solution to problem (P3) can be uniquely constructed based on (30). To sum up, with initial value  $(\hat{x}^{t*}(0), \hat{y}^{t*}(0)) = \mathbf{D}_1 = (w_{1,x}, w_{1,y})$ , the optimal solution of (P3) with  $m < \rho_{\min}(r_1 + r_2)$  is constructed as



(a) Constructed ropes with different absolute values of initial tension at  $D_1$ . (b) Constructed ropes with different initial tension angles and already optimized absolute value.

Fig. 5. Monotonic effects of initial rope tension at  $D_1$  on the constructed ropes.

$$(\hat{x}^*(s), \hat{y}^*(s)) = \left( \int_0^s \frac{-A_1^*(s)}{\sqrt{A_1^*(s)^2 + A_2^*(s)^2}} ds + w_{1,x}, \int_0^s \frac{-A_2^*(s)}{\sqrt{A_1^*(s)^2 + A_2^*(s)^2}} ds + w_{1,y} \right), \quad (31)$$

$$\rho^*(s) = \rho_{\min}, \quad \forall s \in [0, S'^* \triangleq \frac{m}{\rho_{\min}}]. \quad (32)$$

Equivalently, the optimal UAV trajectory  $\{x^*(t), y^*(t)\}$  for original problem (OP) in case of  $T < \frac{r_1 + r_2}{V}$  can be constructed, as shown in Fig. 4(b). It is given by

$$(x^*(t), y^*(t)) = (\hat{x}^*(Vt), \hat{y}^*(Vt)), \quad \text{where } V = 1/\rho_{\min}. \quad (33)$$

## V. OPTIMAL INITIAL ROPE TENSION DESIGN

So far, the optimal solution of UAV trajectory has been constructed. However, from the above results, we learn that to obtain the optimal solution with insufficient rope mass  $m < \rho_{\min}(r_1 + r_2)$ , it is essential to design the optimal rope tension  $Q_0^*$  at  $D_1$ . Actually, the optimal rope tension can be quickly obtained by simply greedily searching the optimal values of two parameters, i.e., the absolute value  $Q_0$  and the tension angle  $\alpha$ . More specifically, with a fixed angle  $\alpha$  of initial tension at  $D_1$ , a larger absolute value  $Q_0$  makes the constructed rope always closer to the centre  $D_0$ , as implied in Fig. 5(a). Therefore, for any given angle  $\alpha$ , there exists a unique absolute value  $Q_0^*(\alpha)$  making the rope exactly pass the destination  $D_2$ . More importantly, this value  $Q_0^*(\alpha)$  can be simply found by fixing  $\alpha$  and greedily searching over the absolute value  $Q_0$ . On the other hand, with  $Q_0 = Q_0^*(\alpha)$ , the rope length between  $D_1$  and  $D_2$  is actually monotonically increasing with respect to the angle  $\alpha$ , as shown in Fig. 5(b). Hence, with given  $Q_0 = Q_0^*(\alpha)$ , the optimal initial tension  $Q_0^*$  can be uniquely found by further greedily searching over angle  $\alpha$ .

In this section, we provide rigorous proofs for the above stated monotonic impacts of absolute value  $Q_0$  and tension angle  $\alpha$ , in purpose of guaranteeing the global optimality of our design. To start with, we first derive a closed-form rope shape expression in the polar coordinate system, based on which the effect analysis for initial rope tension can be significantly facilitated. Then, the impact of the initial rope tension on constructed rope will be addressed subsequently.

### A. Closed-Form Expression in Polar Coordinate System

We first consider a polar coordinate system  $(r, \varphi)$  with original point defined as the center  $\mathbf{D}_0$  of APF, as shown in Fig. 6(a). In the polar coordinate system, the coordinates of two rope endpoints, namely points  $\mathbf{D}_1$  and  $\mathbf{D}_2$  with Cartesian coordinates  $(w_{1,x}, w_{1,y})$  and  $(w_{2,x}, w_{2,y})$ , are respectively given by  $(r_1, \varphi_1)$  and  $(r_2, \varphi_2)$ . Without loss of generality, we assume  $\varphi_2 > \varphi_1$ . In addition, the rope shape  $\{\hat{x}'(s), \hat{y}'(s)\}$  is transformed to  $\{r(s), \varphi(s)\}$ , according to the following relations

$$\hat{x}'(s) = r(s) \cos \varphi(s), \quad \hat{y}'(s) = r(s) \sin \varphi(s). \quad (34)$$

Note that with any initial rope tension  $\mathbf{Q}_0$  at  $\mathbf{D}_1$ , i.e., including an absolute value  $Q_0 = |\mathbf{Q}_0|$  and angle  $\alpha$ , the rope shape  $\{\hat{x}'(s), \hat{y}'(s)\}$  can be uniquely determined by replacing  $|\mathbf{Q}_0^*|$  and  $\alpha^*$  respectively with  $|\mathbf{Q}_0|$  and  $\alpha$  given in (25) and (26). An example generated rope shape  $(r(s), \varphi(s))$  is shown in Fig. 6(a). It should be mentioned that with a random initial rope tension  $\mathbf{Q}_0$ , the generated rope shape does not necessarily pass through the other endpoint  $\mathbf{D}_2$ .

Note that the optimal rope shape  $\{\hat{x}'^*(s), \hat{y}'^*(s)\}$  is strictly limited in the triangle area formed by  $\mathbf{D}_i$ ,  $i \in \{0, 1, 2\}$ . Accordingly, the angle  $\alpha^*$  of optimal tension  $\mathbf{Q}_0^*$  is bounded in interval  $[\arctan \frac{w_{2,y}-w_{1,y}}{w_{2,x}-w_{1,x}}, \varphi_1]$ . Therefore, we assume  $\alpha \in [\arctan \frac{w_{2,y}-w_{1,y}}{w_{2,x}-w_{1,x}}, \varphi_1]$ .

In the polar coordinate system, for any given initial rope tension  $\mathbf{Q}_0$  at  $\mathbf{D}_1$ , we have the following relation for the generated rope shape  $\{r(s), \varphi(s)\}$ ,

$$\frac{A_2(s)}{A_1(s)} = \frac{d\hat{x}'(s)}{d\hat{y}'(s)} = \frac{d(r(s) \cos \varphi(s))}{d(r(s) \sin \varphi(s))} = \frac{r(s) \frac{d\varphi(s)}{dr(s)} + \tan \varphi(s)}{1 - r(s) \frac{d\varphi(s)}{dr(s)} \tan \varphi(s)}, \quad (35)$$

where  $A_1(s)$  and  $A_2(s)$  are modified equations (25) and (26) by replacing  $|\mathbf{Q}_0^*|$  and  $\alpha^*$  respectively with  $|\mathbf{Q}_0|$  and  $\alpha$ . The expressions of  $A_1(s)$  and  $A_2(s)$  in the polar coordinate system are given by

$$A_1(s) = Q_0 \cos \alpha + \int_0^s g(r(s_0)) \rho_{\min}(-\cos \varphi(s_0)) ds_0, \quad (36)$$

$$A_2(s) = Q_0 \sin \alpha + \int_0^s g(r(s_0)) \rho_{\min}(-\sin \varphi(s_0)) ds_0, \quad (37)$$

where  $g(r(s))$  is defined as the absolute value of fore field with distance to center point  $r(s)$ , i.e.,  $g(r(s)) = |\mathbf{g}(x, y)|$ , when  $\sqrt{x^2 + y^2} = r(s)$ . And from the equation (35), we can also obtain that

$$r(s) \frac{d\varphi(s)}{dr(s)} = \frac{\frac{A_2(s)}{A_1(s)} - \tan \varphi(s)}{1 + \frac{A_2(s)}{A_1(s)} \tan \varphi(s)}. \quad (38)$$

In the following, in order to gain a deep insight of the relation between  $r(s)$  and  $\varphi(s)$  with given  $\mathbf{Q}_0$ , we make efforts to construct an equation containing only variables  $r(s)$  and  $\varphi(s)$ . To facilitate the formulation of generated rope shape in the polar coordinate system, we first introduce a Lemma 3 regarding the relation between  $A_1(s)$  and  $A_2(s)$  with a given  $\mathbf{Q}_0$ .

**Lemma 3.** For a given  $\mathbf{Q}_0$ , in the generated  $\{r(s), \varphi(s)\}$  from (38), the value of  $A_1(s)r(s) \sin \varphi(s) - A_2(s)r(s) \cos \varphi(s)$  is constant in  $s$ . Namely,

$$A_1(s)r(s) \sin \varphi(s) - A_2(s)r(s) \cos \varphi(s) = r_1 Q_0 \sin(\varphi_1 - \alpha) \triangleq \hat{Q}_0. \quad (39)$$

*Proof.* We prove the lemma by studying the first-order derivative of the term  $A_1(s)r(s) \sin \varphi(s) - A_2(s)r(s) \cos \varphi(s)$  in  $s$ , which is obtained as

$$\begin{aligned} & \frac{dA_1(s)r(s) \sin \varphi(s) - A_2(s)r(s) \cos \varphi(s)}{ds} \\ &= g(r(s))\rho_{\min}(-\cos \varphi(s))r(s) \sin \varphi(s) - g(r(s))\rho_{\min}(-\sin \varphi(s))r(s) \cos \varphi(s) \\ & \quad + (A_1(s) \sin \varphi(s) - A_2(s) \cos \varphi(s)) \frac{dr(s)}{ds} + (A_1(s) \cos \varphi(s) + A_2(s) \sin \varphi(s))r(s) \frac{d\varphi(s)}{ds}. \end{aligned} \quad (40)$$

Considering the relation (38) between  $\frac{dr(s)}{ds}$  and  $\frac{d\varphi(s)}{ds}$ , the above derivative becomes zero, and the constant value of  $A_1(s)r(s) \sin \varphi(s) - A_2(s)r(s) \cos \varphi(s)$  can be derived to be equal to its initial value  $A_1(0)r(0) \sin \varphi(0) - A_2(0)r(0) \cos \varphi(0) = r_1 Q_0 \sin(\varphi_1 - \alpha) \triangleq \hat{Q}_0$ .  $\square$

**Remark.** Note that Lemma 3 substantially represents the zero net torque requirement in the equilibrium state. The torque is taken with respect to the origin point and the value  $\hat{Q}_0$  is actually the resulted torque by  $\mathbf{Q}_0$  with respect to the origin  $\mathbf{D}_0$ . As the force field in APF is always towards origin  $\mathbf{D}_0$ , the torque resulted from  $\mathbf{Q}(s)$ , namely  $A_1(s)r(s) \sin \varphi(s) - A_2(s)r(s) \cos \varphi(s)$ , remains to be a constant.

Combining (35) and (39), we find that  $A_1(s)$  and  $A_2(s)$  can be completely represented by  $r(s)$ ,  $\varphi(s)$  and  $\frac{d\varphi(s)}{dr(s)}$ , namely

$$A_1(s) = -\frac{\hat{Q}_0 \left(1 - r(s) \frac{d\varphi(s)}{dr(s)} \tan \varphi(s)\right)}{r(s)^2 \frac{d\varphi(s)}{dr(s)} \frac{1}{\cos \varphi(s)}}, \quad A_2(s) = -\frac{\hat{Q}_0 \left(r(s) \frac{d\varphi(s)}{dr(s)} + \tan \varphi(s)\right)}{r(s)^2 \frac{d\varphi(s)}{dr(s)} \frac{1}{\cos \varphi(s)}}. \quad (41)$$

Then, by taking derivative of both sides of (38) to  $s$ , we can correspondingly get an expression of  $\frac{d\left(r(s) \frac{d\varphi(s)}{dr(s)}\right)}{ds}$  which contains the function term of  $A_1(s)$  and  $A_2(s)$ . However, according to (41), the expression of  $\frac{d\left(r(s) \frac{d\varphi(s)}{dr(s)}\right)}{ds}$  can be simplified after a series of reformulation. Finally, we have

$$\frac{d\left(r(s) \frac{d\varphi(s)}{dr(s)}\right)}{ds} = -\frac{d\varphi(s)}{ds} \left( \left(r(s) \frac{d\varphi(s)}{dr(s)}\right)^2 + 1 \right) - \left(r(s) \frac{d\varphi(s)}{dr(s)}\right)^2 \frac{g(r(s))\rho_{\min}r(s)}{\hat{Q}_0}, \quad (42)$$

which does not contain any terms of  $A_1(s)$  and  $A_2(s)$ . In the same way, we obtain that

$$\frac{dr(s)}{ds} = \frac{-A_1(s) \cos \varphi(s) - A_2(s) \sin \varphi(s)}{\sqrt{A_1(s)^2 + A_2(s)^2}} = \frac{\text{sgn}\left(\frac{dr(s)}{ds}\right)}{\sqrt{\left(r(s) \frac{d\varphi(s)}{dr(s)}\right)^2 + 1}}, \quad (43)$$

where  $\text{sgn}\left(\frac{dr(s)}{ds}\right)$  indicates the sign of  $\frac{dr(s)}{ds}$ . Thus, by combining the above two equations, we have



$$\frac{d\left(r(s)\frac{d\varphi(s)}{dr(s)}\right)}{dr(s)} = -\frac{d\varphi(s)}{dr(s)} \left( \left(r(s)\frac{d\varphi(s)}{dr(s)}\right)^2 + 1 \right) - \operatorname{sgn}\left(\frac{dr(s)}{ds}\right) \left(r(s)\frac{d\varphi(s)}{dr(s)}\right)^2 \sqrt{\left(r(s)\frac{d\varphi(s)}{dr(s)}\right)^2 + 1} \frac{g(r(s))\rho_{\min}r(s)}{\hat{Q}_0}. \quad (44)$$

Note that besides  $r(s)$  and  $\varphi(s)$ , the only remaining variable in the above equation is the variable  $s$  in the discontinuous function  $\operatorname{sgn}(\frac{dr(s)}{ds})$ . To further simplify the equation, we first discuss the sign of  $\frac{d\varphi(s)}{ds}$ . Following the same process of obtaining  $\frac{dr(s)}{ds}$ ,  $\frac{d\varphi(s)}{ds}$  is given by

$$\frac{d\varphi(s)}{ds} = \frac{A_1(s)r(s)\sin\varphi(s) - A_2(s)r(s)\cos\varphi(s)}{r(s)^2\sqrt{A_1(s)^2 + A_2(s)^2}} = \frac{r_1Q_0\sin(\varphi_1 - \alpha)}{r(s)^2\sqrt{A_1(s)^2 + A_2(s)^2}}. \quad (45)$$

It is already assumed that the angle  $\alpha$  is limited in interval  $\alpha \in [\arctan \frac{w_{2,y}-w_{1,y}}{w_{2,x}-w_{1,x}}, \varphi_1]$  and we have  $\arctan \frac{w_{2,y}-w_{1,y}}{w_{2,x}-w_{1,x}} > \varphi_1 - \pi$  to make sure  $\varphi_2 > \varphi_1$ . Thus, we always have  $\frac{d\varphi(s)}{ds} > 0$ ,  $\frac{d(r(s)\frac{d\varphi(s)}{dr(s)})}{ds} < 0$  and correspondingly,  $\operatorname{sgn}\left(\frac{dr(s)}{ds}\right) = \operatorname{sgn}\left(\frac{dr(s)}{d\varphi(s)}\right) \operatorname{sgn}\left(\frac{d\varphi(s)}{ds}\right) = \operatorname{sgn}\left(\frac{dr(s)}{d\varphi(s)}\right)$ . Subsequently, the equation (44) can be reformulated as a form with only variables  $r(s)$  and  $\varphi(s)$  involved, namely

$$\frac{d\left(\sqrt{\left(\frac{1}{r(s)}\frac{dr(s)}{d\varphi(s)}\right)^2 + 1}\right)}{dr(s)} = \frac{1}{r(s)} \sqrt{\left(\frac{1}{r(s)}\frac{dr(s)}{d\varphi(s)}\right)^2 + 1} + \frac{g(r(s))\rho_{\min}r(s)}{\hat{Q}_0}. \quad (46)$$

We observe that the equation (46) is actually a linear differential equation of  $\sqrt{\left(\frac{1}{r(s)}\frac{dr(s)}{d\varphi(s)}\right)^2 + 1}$  with respect to  $r(s)$ . According to [27], we can build the solution for equation (46) as

$$\sqrt{\left(\frac{1}{r(s)}\frac{dr(s)}{d\varphi(s)}\right)^2 + 1} = \frac{\rho_{\min}}{\hat{Q}_0} r(s) \int_{r_1}^{r(s)} g(r_0) dr_0 + \frac{r(s)}{r_1} \frac{1}{\sin(\varphi_1 - \alpha)}, \quad (47)$$

where the initial value is  $\sqrt{\left(\frac{1}{r(s)}\frac{dr(s)}{d\varphi(s)}\right)^2 + 1} \Big|_{s=0} = \frac{1}{\sin(\varphi_1 - \alpha)}$ . And a more visualized result for  $\frac{dr(s)}{d\varphi(s)}$  is

$$\left|\frac{dr(s)}{d\varphi(s)}\right| = r(s) \sqrt{\left(\frac{\rho_{\min}}{\hat{Q}_0} r(s) \int_{r_1}^{r(s)} g(r_0) dr_0 + \frac{r(s)}{r_1} \frac{1}{\sin(\varphi_1 - \alpha)}\right)^2 - 1}. \quad (48)$$

Moreover, with the conclusions  $\frac{d\varphi(s)}{ds} > 0$  and  $\frac{d(r(s)\frac{d\varphi(s)}{dr(s)})}{ds} < 0$ , we obtain that

$$\frac{d\left(\frac{dr(s)}{d\varphi(s)}\right)}{d\varphi(s)} = \frac{1}{\frac{d\varphi(s)}{ds}} \left( \frac{d\varphi(s)}{ds} - \frac{d\left(r(s)\frac{d\varphi(s)}{dr(s)}\right)}{ds} \right) \frac{1}{r(s)\left(\frac{d\varphi(s)}{dr(s)}\right)^2} > 0, \quad (49)$$

so that  $r(s)$  is proved to be convex in  $\varphi(s)$ . Then based on (48), we can directly focus on the variation tendency of  $r(s)$  to  $\varphi(s)$ . Note that different initial value and sign of  $\frac{dr(s)}{d\varphi(s)}$  at  $s = 0$  will lead to different variation tendency of  $r(s)$ . Therefore, we next formulate the closed-form expression of  $\varphi(s)$  in  $r(s)$ , respectively under two cases regarding the initial sign of  $\frac{dr(s)}{d\varphi(s)}$ .

- When  $\frac{dr(s)}{d\varphi(s)} \Big|_{s=0} \geq 0$ , as  $r(s)$  is convex in  $\varphi(s)$ , we have  $\forall s \geq 0$ ,  $\frac{dr(s)}{d\varphi(s)} \geq 0$  holds and both



**Lemma 4.** With a fixed tension angle  $\alpha \in (\varphi_1 - \pi, \varphi_1)$ , in the generated rope shape  $\{r(s), \varphi(s)\}$ ,  $\forall \varphi_0 > \varphi_1$ , the corresponding  $r(s)$  when  $\varphi(s) = \varphi_0$  is monotonically decreasing with respect to tension value  $Q_0$ .

*Proof.* As indicated by (39), with given  $\alpha$ ,  $\hat{Q}_0$  is positively proportional to  $Q_0$ . For facilitation, we study the effect of  $\hat{Q}_0$  instead, and the same conclusion will be proved. From the previous discussions, we have different closed-form relations between  $r(s)$  and  $\varphi(s)$ , i.e., equations (50) and (52), corresponding to different initial value of  $\frac{dr(s)}{d\varphi(s)}$ . Hence, the effect of  $\hat{Q}_0$  should also be investigated in two different cases.

**Case I:**  $\frac{dr(s)}{d\varphi(s)} \Big|_{s=0} \geq 0$ .  $\forall \varphi_0 > \varphi_1$ , when  $\varphi(s) = \varphi_0$ , we have  $r(s) > r_1$  and

$$\int_{r_1}^{r(s)} \frac{dr_0}{r_0 \sqrt{\left( \frac{\rho_{\min}}{\hat{Q}_0} r_0 \int_{r_1}^{r_0} g(r'_0) dr'_0 + \frac{r_0}{r_1} \frac{1}{\sin(\varphi_1 - \alpha)} \right)^2 - 1}} = \varphi_0 - \varphi_1. \quad (53)$$

As the right side of the above equation is a constant, by taking differentiation, we can obtain the relation between  $r(s)$  and  $\hat{Q}_0$ :

$$\frac{dr(s)}{d\hat{Q}_0} = - \frac{H_0(\hat{Q}_0, \alpha, r_1, r(s))}{r(s) \sqrt{\left( \frac{\rho_{\min}}{\hat{Q}_0} r(s) \int_{r_1}^{r(s)} g(r'_0) dr'_0 + \frac{r(s)}{r_1} \frac{1}{\sin(\varphi_1 - \alpha)} \right)^2 - 1}}. \quad (53)$$

where the expression  $H_0(\hat{Q}_0, \alpha, r', r'')$  is defined as the following form for simplification:

$$H_0(\hat{Q}_0, \alpha, r', r'') = \int_{r'}^{r''} \frac{\left( \frac{\rho_{\min}}{\hat{Q}_0} r_0 \int_{r_1}^{r_0} g(r'_0) dr'_0 + \frac{r_0}{r_1} \frac{1}{\sin(\varphi_1 - \alpha)} \right) \left( \frac{\rho_{\min}}{\hat{Q}_0^2} r_0 \int_{r_1}^{r_0} g(r'_0) dr'_0 \right)}{r_0 \left( \sqrt{\left( \frac{\rho_{\min}}{\hat{Q}_0} r_0 \int_{r_1}^{r_0} g(r'_0) dr'_0 + \frac{r_0}{r_1} \frac{1}{\sin(\varphi_1 - \alpha)} \right)^2 - 1}} \right)^3} dr_0 \quad (54)$$

Therefore, as  $r(s) > r_1$  and  $r_0 \in [r_1, r(s)]$ , we have  $H_0(\hat{Q}_0, \alpha, r_1, r(s)) > 0$  and  $\frac{dr(s)}{d\hat{Q}_0} < 0$  for  $\varphi(s) = \varphi_0$ . A larger  $\hat{Q}_0$ , i.e., larger  $Q_0$ , results in a smaller  $r(s)$  for a given  $\varphi(s)$ .

**Case II:**  $\frac{dr(s)}{d\varphi(s)} \Big|_{s=0} < 0$ . If  $\varphi_0 > \varphi_1$  makes  $\frac{dr(s)}{d\varphi(s)} \Big|_{\varphi(s)=\varphi_0} \leq 0$ , according to (52), when  $\varphi(s) = \varphi_0$ ,  $\frac{dr(s)}{d\hat{Q}_0}$  can be obtained to be the same form as (53). Differently, we have  $r(s) < r_1$  and  $r_0 \in [r(s), r_1]$ , which still result in  $H_0(\hat{Q}_0, \alpha, r_1, r(s)) > 0$  and  $\frac{dr(s)}{d\hat{Q}_0} < 0$  for  $\varphi(s) = \varphi_0$ .

If  $\varphi_0 > \varphi_1$  makes  $\frac{dr(s)}{d\varphi(s)} \Big|_{\varphi(s)=\varphi_0} > 0$ , according to (52), when  $\varphi(s) = \varphi_0$ ,  $\frac{dr(s)}{d\hat{Q}_0}$  is given by

$$\frac{dr(s)}{d\hat{Q}_0} = - \frac{2 \frac{dH(\hat{Q}_0, \alpha)}{d\hat{Q}_0} + H_0(\hat{Q}_0, \alpha, r_1, r(s))}{r(s) \sqrt{\left( \frac{\rho_{\min}}{\hat{Q}_0} r(s) \int_{r_1}^{r(s)} g(r'_0) dr'_0 + \frac{r(s)}{r_1} \frac{1}{\sin(\varphi_1 - \alpha)} \right)^2 - 1}}. \quad (55)$$

Obviously, based on previous discussions, if  $\frac{dH(\hat{Q}_0, \alpha)}{d\hat{Q}_0} \geq 0$  for given  $\alpha$ , we will get a conclusion of  $\frac{dr(s)}{d\hat{Q}_0} < 0$  for  $\varphi(s) = \varphi_0$ ,  $\forall \varphi_0 > 0$  for all cases. And  $r(s)$  when  $\varphi(s) = \varphi_0$  can be proved to be monotonically decreasing with respect to  $\hat{Q}_0$ , i.e., monotonically decreasing with respect to  $Q_0$ .

Finally, we prove that  $\frac{dH(\hat{Q}_0, \alpha)}{d\hat{Q}_0} \geq 0$  holds for given  $\alpha$  to finalize the proof. At first,  $r_{\min}$  is dependent in  $\hat{Q}_0$  according to (51), and the derivative is formulated as

$$\frac{dr_{\min}}{d\hat{Q}_0} = \frac{\frac{\rho_{\min}}{\hat{Q}_0^2} r_{\min} \int_{r_1}^{r_{\min}} g(r_0) dr_0}{\frac{1}{r_{\min}} + \frac{\rho_{\min}}{\hat{Q}_0} r_{\min} g(r_{\min})} < 0, \text{ as } r_{\min} < r_1. \quad (56)$$

Then, the derivative of function  $H(\hat{Q}_0, \alpha)$  over  $\hat{Q}_0$  is formulated as

$$\frac{dH(\hat{Q}_0, \alpha)}{d\hat{Q}_0} = \frac{-1}{r_{\min} \sqrt{\left( \frac{\rho_{\min}}{\hat{Q}_0} r_{\min} \int_{r_1}^{r_{\min}} g(r_0) dr_0 + \frac{r_{\min}}{r_1} \frac{1}{\sin(\varphi_1 - \alpha)} \right)^2 - 1}} \frac{dr_{\min}}{d\hat{Q}_0} - H_0(\hat{Q}_0, \alpha, r_1, r_{\min}). \quad (57)$$

Taking the relation between  $r_{\min}$  and  $\hat{Q}_0$  (51) into account,  $\frac{dH(\hat{Q}_0, \alpha)}{d\hat{Q}_0}$  is indeed the difference between two positive infinite values. However, we can still get the sign of  $\frac{dH(\hat{Q}_0, \alpha)}{d\hat{Q}_0}$  via some tricks.

By introducing a variable  $z$

$$z(r_0) = \left( \frac{\rho_{\min}}{\hat{Q}_0} r_0 \int_{r_1}^{r_0} g(r'_0) dr'_0 + \frac{r_0}{r_1} \frac{1}{\sin(\varphi_1 - \alpha)} \right)^2 - 1, \quad (58)$$

and a sufficiently small value  $\epsilon$  for representing  $\left( \frac{\rho_{\min}}{\hat{Q}_0} r_{\min} \int_{r_1}^{r_{\min}} g(r_0) dr_0 + \frac{r_{\min}}{r_1} \frac{1}{\sin(\varphi_1 - \alpha)} \right)^2 - 1$ , we have the reformulated  $\frac{dH(\hat{Q}_0, \alpha)}{d\hat{Q}_0}$  as

$$\frac{dH(\hat{Q}_0, \alpha)}{d\hat{Q}_0} = \lim_{\epsilon \rightarrow 0^+} \left( \frac{-1}{r_{\min} \sqrt{\epsilon}} \frac{dr_{\min}}{d\hat{Q}_0} - \int_{z(r_1)}^{\epsilon} \frac{\frac{1}{2r_0} \frac{\rho_{\min}}{\hat{Q}_0^2} r_0 \int_{r_1}^{r_0} g(r'_0) dr'_0}{\frac{\rho_{\min}}{\hat{Q}_0} \int_{r_1}^{r_0} g(r'_0) dr'_0 + \frac{1}{r_1} \frac{1}{\sin(\varphi_1 - \alpha)} + \frac{\rho_{\min}}{\hat{Q}_0} r_0 g(r_0)} z^{-\frac{3}{2}} dz \right), \quad (59)$$

where  $r_0$  is also a function of  $z$  and  $z(r_{\min}) = 0$ . Next, we compare it with  $\epsilon^{-1}$ , namely

$$\begin{aligned} & \lim_{\epsilon \rightarrow 0^+} \frac{\frac{-1}{r_{\min} \sqrt{\epsilon}} \frac{dr_{\min}}{d\hat{Q}_0} - \int_{z(r_1)}^{\epsilon} \frac{\frac{1}{2r_0} \frac{\rho_{\min}}{\hat{Q}_0^2} r_0 \int_{r_1}^{r_0} g(r'_0) dr'_0}{\frac{\rho_{\min}}{\hat{Q}_0} \int_{r_1}^{r_0} g(r'_0) dr'_0 + \frac{1}{r_1} \frac{1}{\sin(\varphi_1 - \alpha)} + \frac{\rho_{\min}}{\hat{Q}_0} r_0 g(r_0)} z^{-\frac{3}{2}} dz}{\epsilon^{-1}} \\ &= \lim_{\epsilon \rightarrow 0^+} \left( \frac{-\sqrt{\epsilon} \frac{dr_{\min}}{d\hat{Q}_0}}{r_{\min}} + \frac{\frac{\sqrt{\epsilon}}{2r_{\min}} \frac{\rho_{\min}}{\hat{Q}_0^2} r_{\min} \int_{r_1}^{r_{\min}} g(r'_0) dr'_0}{\frac{\rho_{\min}}{\hat{Q}_0} \int_{r_1}^{r_{\min}} g(r'_0) dr'_0 + \frac{1}{r_1} \frac{1}{\sin(\varphi_1 - \alpha)} + \frac{\rho_{\min}}{\hat{Q}_0} r_{\min} g(r_{\min})} \right) \\ &= \lim_{\epsilon \rightarrow 0^+} \frac{-\sqrt{\epsilon} \frac{dr_{\min}}{d\hat{Q}_0}}{2r_{\min}} = 0_+, \text{ as } \frac{dr_{\min}}{d\hat{Q}_0} < 0. \end{aligned} \quad (60)$$

As  $\lim_{\epsilon \rightarrow 0^+} \frac{1}{\epsilon} = +\infty$ , it is eventually proved that  $\frac{dH(\hat{Q}_0, \alpha)}{d\hat{Q}_0} \geq 0$  holds for a fixed angle  $\alpha$ .

To more intuitively show the effects of initial tension value  $Q_0$  with given  $\alpha$ , examples for both Case I and Case II are displayed in Fig. 6(b). For Case I, two rope shapes are generated by  $\mathbf{Q}_1$  and  $\mathbf{Q}_2$  ( $|\mathbf{Q}_2| > |\mathbf{Q}_1|$ ) with  $\alpha = \alpha_1$ . And the examples of the generated rope shapes by  $\mathbf{Q}_3$  and  $\mathbf{Q}_4$  ( $|\mathbf{Q}_4| > |\mathbf{Q}_3|$ ) with  $\alpha = \alpha_2$  belong to Case II.  $\square$

According to Lemma 4, for given  $\alpha$ , a larger value of  $Q_0$  always results in a generated rope closer to  $\mathbf{D}_0$ . Thus, through greedily searching of  $Q_0$ , the unique corresponding  $Q_0 = Q_0^*(\alpha)$  can be found, with which the generated rope  $\{r(s), \varphi(s)\}$  passes through the destination  $\mathbf{D}_2(r_2, \varphi_2)$ .

### C. Effect of $\alpha$ on Generated Rope Shape

On the other hand, the angle  $\alpha$  for initial rope tension can also result in a monotonic effect on the generated rope. Regarding the effect of initial tension angle  $\alpha$ , we have the following Lemma 5. In other word, with a fixed  $\hat{Q}_0$ , i.e., fixed value of  $r_1 Q_0 \sin(\varphi_1 - \alpha)$ , a larger initial tension angle  $\alpha$  results in a rope shape closer to the center  $\mathbf{D}_0$ .

**Lemma 5.** *With a fixed value of  $\hat{Q}_0$  (not  $Q_0$ ) in the initial tension  $\mathbf{Q}_0$ , in the generated rope shape  $\{r(s), \varphi(s)\}$ ,  $\forall \varphi_0 > \varphi_1$ , the corresponding  $r(s)$  when  $\varphi(s) = \varphi_0$  is monotonically decreasing with respect to the tension angle  $\alpha \in (\varphi_1 - \pi, \varphi_1)$ .*

*Proof.* According to the closed-form expression of generated rope shape in (50) and (52), we prove the lemma by distinguishing the following two cases.

**Case I:** When  $\alpha \in (\varphi_1 - \pi, \varphi_1 - \frac{\pi}{2}]$ , we have  $\frac{dr(s)}{d\varphi(s)} \Big|_{s=0} \geq 0$ , so that the relation (50) holds. Similarly, with a fixed value of  $\hat{Q}_0$ , we have  $\frac{dr(s)}{d\sin(\varphi_1 - \alpha)}$  described as

$$\frac{dr(s)}{d\sin(\varphi_1 - \alpha)} = - \frac{H_1(\hat{Q}_0, \alpha, r_1, r(s))}{r(s) \sqrt{\left( \frac{\rho_{\min}}{\hat{Q}_0} r(s) \int_{r_1}^{r(s)} g(r'_0) dr'_0 + \frac{r(s)}{r_1} \frac{1}{\sin(\varphi_1 - \alpha)} \right)^2 - 1}}. \quad (61)$$

where the expression  $H_1(\hat{Q}_0, \alpha, r', r'')$  is defined as

$$H_1(\hat{Q}_0, \alpha, r', r'') = \int_{r'}^{r''} \frac{\left( \frac{\rho_{\min}}{\hat{Q}_0} r_0 \int_{r_1}^{r_0} g(r'_0) dr'_0 + \frac{r_0}{r_1} \frac{1}{\sin(\varphi_1 - \alpha)} \right) \left( \frac{r_0}{r_1} \frac{1}{\sin^2(\varphi_1 - \alpha)} \right)}{r_0 \left( \sqrt{\left( \frac{\rho_{\min}}{\hat{Q}_0} r_0 \int_{r_1}^{r_0} g(r'_0) dr'_0 + \frac{r_0}{r_1} \frac{1}{\sin(\varphi_1 - \alpha)} \right)^2 - 1}} \right)^3} dr_0 \quad (62)$$

Therefore, when  $\varphi(s) = \varphi_0 > \varphi_1$ , we have  $r(s) > r_1$  and accordingly  $\frac{dr(s)}{d\sin(\varphi_1 - \alpha)} < 0$ , i.e.,

$$\frac{dr(s)}{d\alpha} = \frac{dr(s)}{d\sin(\varphi_1 - \alpha)} (-\cos(\varphi_1 - \alpha)) < 0. \quad (63)$$

**Case II:** When  $\alpha \in (\varphi_1 - \frac{\pi}{2}, \varphi_1)$ , we have (52) holds. If  $\varphi_0 > \varphi_1$  makes  $\frac{dr(s)}{d\varphi(s)} \Big|_{\varphi(s)=\varphi_0} \leq 0$ , according to (52), when  $\varphi(s) = \varphi_0$ ,  $\frac{dr(s)}{d\sin(\varphi_1 - \alpha)}$  can be obtained to be the same form as (61). Differently, we have  $r(s) < r_1$ , which results in  $\frac{dr(s)}{d\sin(\varphi_1 - \alpha)} > 0$ , namely  $\frac{dr(s)}{d\alpha} < 0$  since  $\cos(\varphi_1 - \alpha) > 0$  holds for  $\alpha \in (\varphi_1 - \frac{\pi}{2}, \varphi_1)$ .

If  $\varphi_0 > \varphi_1$  makes  $\frac{dr(s)}{d\varphi(s)} \Big|_{\varphi(s)=\varphi_0} > 0$ , according to (52), when  $\varphi(s) = \varphi_0$ , with a fixed  $\hat{Q}_0$ ,  $\frac{dr(s)}{d\sin(\varphi_1 - \alpha)}$  can be obtained as

$$\frac{dr(s)}{d\sin(\varphi_1 - \alpha)} = - \frac{H_2(\hat{Q}_0, \alpha, r(s)) + H_1(\hat{Q}_0, \alpha, 2r(s), r(s))}{r(s) \sqrt{\left( \frac{\rho_{\min}}{\hat{Q}_0} r(s) \int_{r_1}^{r(s)} g(r'_0) dr'_0 + \frac{r(s)}{r_1} \frac{1}{\sin(\varphi_1 - \alpha)} \right)^2 - 1}}. \quad (64)$$

where for simplified denotation, the function  $H_2(\hat{Q}_0, \alpha, r(s))$  is defined as

$$H_2(\hat{Q}_0, \alpha, r(s)) = \frac{-2}{r_{\min} \sqrt{\left( \frac{\rho_{\min}}{\hat{Q}_0} r_{\min} \int_{r_1}^{r_{\min}} g(r_0) dr_0 + \frac{r_{\min}}{r_1} \frac{1}{\sin(\varphi_1 - \alpha)} \right)^2 - 1}} \frac{dr_{\min}}{d \sin(\varphi_1 - \alpha)} + H_1(\hat{Q}_0, \alpha, r_{\min}, r_1) + H_1(\hat{Q}_0, \alpha, r_{\min}, 2r(s)), \quad (65)$$

$$\frac{dr_{\min}}{d \sin(\varphi_1 - \alpha)} = \frac{\frac{r_{\min}}{r_1} \frac{1}{\sin^2(\varphi_1 - \alpha)}}{\frac{1}{r_{\min}} + \frac{\rho_{\min}}{\hat{Q}_0} r_{\min} g(r_{\min})} > 0. \quad (66)$$

Following the same process in the proof of Lemma 4, by introducing  $z(r)$  in (58) and a variable  $\epsilon$ , we can find that  $H_2(\hat{Q}_0, \alpha, r(s)) \leq 0$ . Since  $H_1(\hat{Q}_0, \alpha, 2r(s), r(s)) < 0$  holds, we can obtain that  $\frac{dr(s)}{d \sin(\varphi_1 - \alpha)} > 0$  holds for given  $\hat{Q}_0$ . Subsequently, we obtain that  $\frac{dr(s)}{d\alpha} < 0$  for any given  $\hat{Q}_0$ .

To sum up, for any given fixed  $\hat{Q}_0$ , it holds that  $\frac{dr(s)}{d\alpha} < 0$ ,  $\forall \alpha \in (\varphi_1 - \pi, \varphi_1)$ , i.e.,  $r(s)$  is strictly monotonically decreasing with respect to  $\alpha$ .  $\square$

#### D. Relation Between $\alpha$ and Total Rope Length

Based on Lemma 4 and Lemma 5 which respectively show the monotonic effects of initial tension value  $Q_0$  and initial tension angle  $\alpha$  on the generated shape, we can obtain a monotonic relation between the tension angle  $\alpha$  and the total rope length  $S$ . This relation is described in Lemma 6.

**Lemma 6.** *When the tension value is  $Q_0 = Q_0^*(\alpha)$ , so that the generated rope shape  $(r(s), \varphi(s))$  starts from  $D_1(r_1, \varphi_1)$  and ends at  $D_2(r_2, \varphi_2)$ , the total rope length between  $D_1$  and  $D_2$  is strictly monotonically increasing with respect to  $\alpha$ .*

*Proof.* We prove the lemma in the following way with three steps: i. first propose a concept of unlimited rope shape, then ii. find the relation between generated ropes with the same endpoints with the assistance of unlimited rope shape (namely no further intersection points between different generated ropes with the same endpoints), and iii. finally complete the proof based on a property of convex bodies.

We start with introducing the concept of unlimited rope shape. Note that given an initial tension  $Q_0$  at point  $D_1$ , the rope shape can be generated on both left side and right side of line  $D_0D_1$ . More specifically, for the sides  $\varphi > \varphi_1$  and  $\varphi < \varphi_1$ , the balanced rope shapes can be generated respectively with initial rope tensions  $Q_0$  and  $-Q_0$ . An example of created unlimited rope shape is shown in Fig. 7(a). In other words, with any given initial rope tension  $Q_0$ , a unique smooth rope shape without endpoints can be correspondingly created.

Then, we prove a statement that for any two different created unlimited rope shapes, there are at most two intersection points. We assume two created unlimited rope shapes have an intersection point  $D_3(r_3, \varphi_3)$ , and the corresponding two rope tensions at  $D_3$  are respectively  $Q_1$  and  $Q_2$  with their tensions  $Q_1, Q_2$  and angles  $\alpha_1, \alpha_2 \in (\varphi_3 - \pi, \varphi_3)$ ,  $\alpha_1 \leq \alpha_2$ . Accordingly, we have

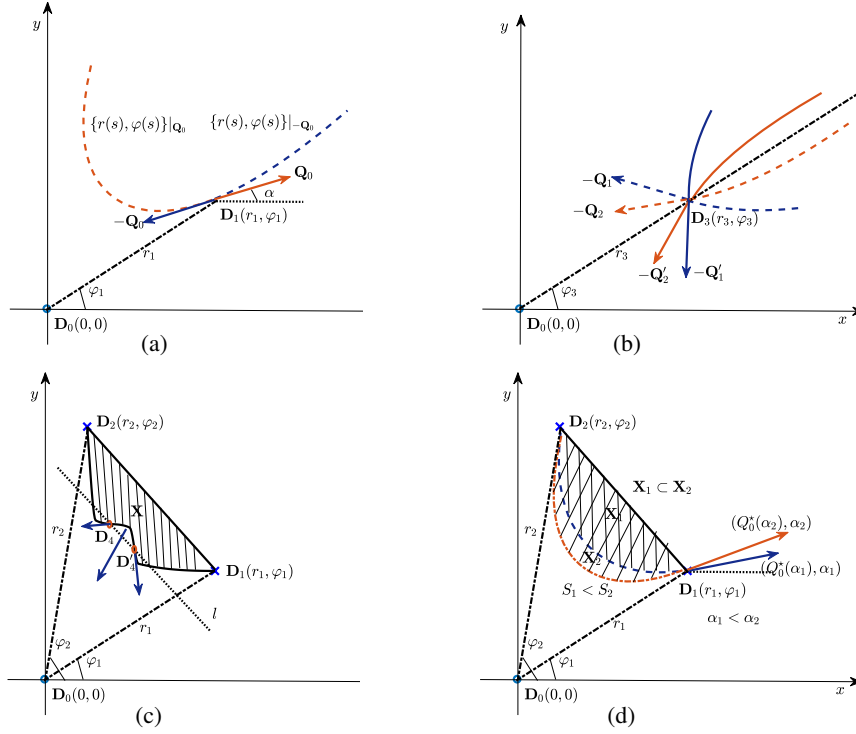


Fig. 7. Example figures for proof of Lemma 6. (a) An example of creating unlimited rope shape. (b) An example of symmetry. (c) An example of unbalanced rope segment within non-convex area  $\mathbf{X}$ . (d) Effect of initial angle  $\alpha$  on the total rope length  $S$ .

$\hat{Q}_1 = r_3 Q_1 \sin(\varphi_3 - \alpha_1)$  and  $\hat{Q}_2 = r_3 Q_2 \sin(\varphi_3 - \alpha_2)$ . Then, we show that there is no intersection point in at least one side, i.e., in either the side of  $\varphi > \varphi_3$  or  $\varphi < \varphi_3$ . In particular, we show this by distinguishing the following these cases satisfying  $\alpha_1 \leq \alpha_2$ .

- If  $\alpha_1 < \alpha_2$  and  $\hat{Q}_1 \leq \hat{Q}_2$  ( $Q_1 \leq \frac{Q_2 \sin(\varphi_3 - \alpha_2)}{\sin(\varphi_3 - \alpha_1)}$ ), according to Lemma 4 and Lemma 5, we have that given  $\varphi > \varphi_3$ , the corresponding distance  $r$  satisfies

$$r|_{(\alpha_2, Q_2)} \stackrel{\text{Lemma 5}}{<} r|_{(\alpha_1, \frac{Q_2 \sin(\varphi_3 - \alpha_2)}{\sin(\varphi_3 - \alpha_1)})} \stackrel{\text{Lemma 4}}{\leq} r|_{(\alpha_1, Q_1)}. \quad (67)$$

Therefore, there is no intersection point in the rope shapes generated from initial tensions  $Q_1$  and  $Q_2$ , i.e., at the side of  $\varphi > \varphi_3$ .

- If  $\alpha_1 < \alpha_2$  and  $\hat{Q}_1 > \hat{Q}_2$ , we study the side where  $\varphi < \varphi_3$ , namely the generated rope segment from initial tensions  $-Q_1$  and  $-Q_2$ . As the angles of initial tensions are located out of the interval  $(\varphi_3 - \pi, \varphi_3)$ , we have that the relations (50) and (52) do not hold any more. However, due to the symmetry of force field (19), we can directly focus on the generated rope from tensions  $-Q'_1(\alpha'_1 = 2\varphi_3 - \alpha_1 - \pi, Q_1)$  and  $-Q'_2(\alpha'_2 = 2\varphi_3 - \alpha_2 - \pi, Q_2)$ , as implied in Fig. 7(b). Clearly,  $\alpha'_1 > \alpha'_2$ . Thus, for given  $\varphi > \varphi_3$ ,

$$r|_{(\alpha'_2, Q_2)} \stackrel{\text{Lemma 5}}{>} r|_{(\alpha'_1, \frac{Q_2 \sin(\varphi_3 - \alpha'_2)}{\sin(\varphi_3 - \alpha'_1)})} \stackrel{\text{Lemma 4}}{>} r|_{(\alpha'_1, Q_1)}. \quad (68)$$

According to the symmetry, we can conclude that there is no intersection point in the rope shapes generated from initial tensions  $-Q_1$  and  $-Q_2$ , i.e., at the side of  $\varphi < \varphi_3$ .

- If  $\alpha_1 = \alpha_2$ , it must hold that  $Q_1 \neq Q_2$ , otherwise  $\mathbf{Q}_1$  and  $\mathbf{Q}_2$  will generate totally same rope shape. As  $Q_1 \neq Q_2$ , the two created rope shape has no intersection as the side of  $\varphi > \varphi_3$  according to Lemma 4.

Hence, the statement “for any two different created unlimited rope shapes, there are at most two intersection points” can be immediately proved by contradiction. In particular, if there are more than two intersection points of two different created unlimited rope shapes, as discussed, the two rope shapes must have the same tensions at one of the intersection point so that these two rope shapes are exactly the same one.

Next, we discuss two initial tensions, i.e.,  $(\alpha_1, Q_0^*(\alpha_1))$  and  $(\alpha_2, Q_0^*(\alpha_2))$  ( $\alpha_1 < \alpha_2$ ), at point  $\mathbf{D}_1$ . Clearly, both two generated ropes pass through points  $\mathbf{D}_1$  and  $\mathbf{D}_2$ . According to the proved statement, there is no other intersection point between  $\mathbf{D}_1$  and  $\mathbf{D}_2$ , namely no intersection point when  $\varphi \in (\varphi_1, \varphi_2)$ . On the other hand, the initial value of  $\frac{dr(s)}{d\varphi(s)}$  is determined by  $\alpha$ , i.e.,  $\frac{dr(s)}{d\varphi(s)} \Big|_{s=0} = -\frac{r_1}{\tan(\varphi_1 - \alpha)}$ . As  $\alpha_1 < \alpha_2$  results in  $-\frac{r_1}{\tan(\varphi_1 - \alpha_1)} > -\frac{r_1}{\tan(\varphi_1 - \alpha_2)}$ , we have

$$r(s)|_{(\alpha_1, Q_0^*(\alpha_1))} > r(s)|_{(\alpha_2, Q_0^*(\alpha_2))}, \text{ when } \varphi(s) \in (\varphi_1, \varphi_2). \quad (69)$$

We denote by  $\mathbf{X}_1$  the area constructed by the line segment  $\mathbf{D}_1\mathbf{D}_2$  and the rope segment generated by initial tension  $(\alpha_1, Q_0^*(\alpha_1))$ , while  $\mathbf{X}_2$  is the area corresponding to initial tension  $(\alpha_2, Q_0^*(\alpha_2))$ , as shown in Fig. 7(d). Therefore, the area  $\mathbf{X}_1$  is a proper subset of  $\mathbf{X}_2$ , i.e.,  $\mathbf{X}_1 \subsetneq \mathbf{X}_2$ . In particular, the intersection of  $\mathbf{X}_1$  and any straight line is convex, otherwise we can find a rope segment which is not in the state of equilibrium, e.g., the rope segment  $\mathbf{D}_4\mathbf{D}'_4$  in Fig. 7(c). The same conclusion holds for  $\mathbf{X}_2$ . Thus, both  $\mathbf{X}_1$  and  $\mathbf{X}_2$  are convex sets.

According to the geometry property of convex sets [28], we have the perimeter of  $\mathbf{X}_2$  is larger than that of  $\mathbf{X}_1$  when  $\mathbf{X}_1 \subsetneq \mathbf{X}_2$ . The perimeters of  $\mathbf{X}_1$  and  $\mathbf{X}_2$  are actually the rope length between  $\mathbf{D}_1$  and  $\mathbf{D}_2$  plus the length of line segment  $\mathbf{D}_1\mathbf{D}_2$ . Therefore, we obtain that for any two initial tensions,  $(\alpha_1, Q_0^*(\alpha_1))$  and  $(\alpha_2, Q_0^*(\alpha_2))$ , if  $\alpha_1 < \alpha_2$  holds, we always have the total rope length corresponding to initial tension  $(\alpha_2, Q_0^*(\alpha_2))$  is larger than that of  $(\alpha_1, Q_0^*(\alpha_1))$ , i.e.,  $S_2 > S_1$ .  $\square$

Therefore, according to Lemma 6, while keeping  $Q_0 = Q_0^*(\alpha)$ , we can find a unique angle  $\alpha^*$  by tuning the value of  $\alpha$ , so that the length of generated rope between  $\mathbf{D}_1$  and  $\mathbf{D}_2$  is exactly equal to  $S^* = \frac{m}{\rho_{\min}}$ . Combining the optimal tension angle  $\alpha^*$  and the corresponding optimal tension value  $Q_0^*(\alpha^*)$ , the optimal initial tension  $\mathbf{Q}_0^*$  can be uniquely constructed, and subsequently we can build the optimal rope solution for (P3) in case of  $m < \rho_{\min}(r_1 + r_2)$ , equivalently the optimal UAV trajectory for (OP) in case of  $T < \frac{r_1 + r_2}{V}$ .

Immediately, we conclude that the optimal rope shape  $\{r^*(s), \varphi^*(s)\}$  generated by the optimal



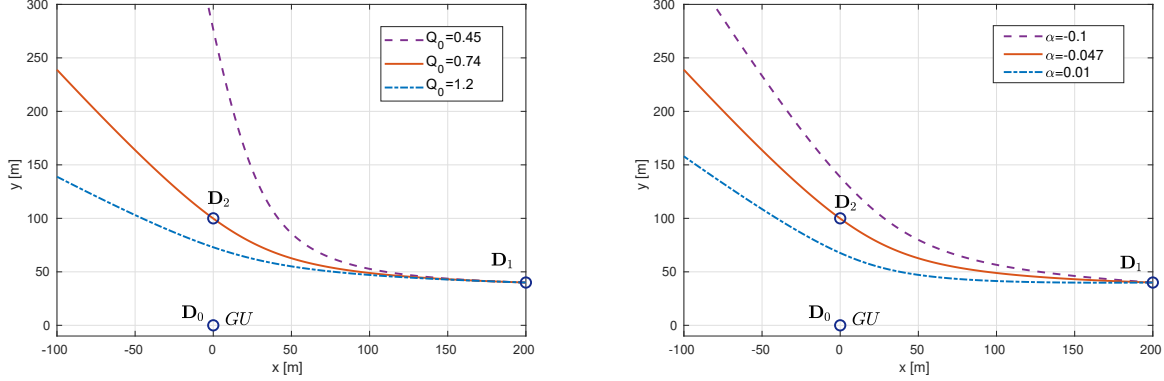


Fig. 8. Observations of the monotonic impact of absolute value  $Q_0$  and angle  $\alpha$  in initial tension.

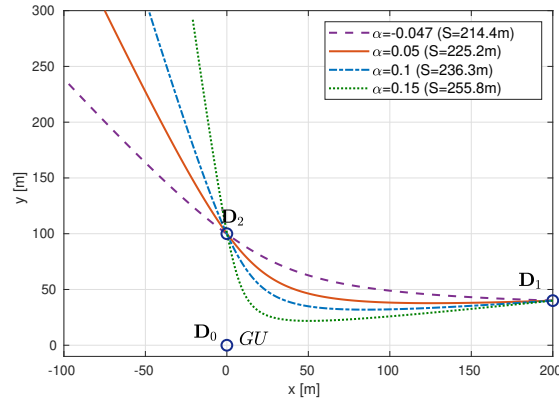


Fig. 9. Generated ropes with different  $\alpha$  and optimized  $Q_0 = Q_0^*(\alpha)$ .

initial tension  $Q_0^*$  satisfies the following two conditions:

- (i).  $\{r^*(s), \varphi^*(s)\}$  passes through the point  $D_2 = (r_2, \varphi_2)$ ;
- (ii). The total rope length of  $\{r^*(s), \varphi^*(s)\}$  is  $\frac{m}{\rho_{\min}}$ .

As a unique  $Q_0$  can be found while satisfying these two conditions, the found  $Q_0$  must be the optimal initial tension, so that the obtained rope solution and equivalent trajectory solution are absolutely optimal.

## VI. SIMULATION RESULTS

In this section, via simulation results, we validate the monotonic impacts of the absolute value  $Q_0$  and angle  $\alpha$  on the generated rope, and evaluate our globally optimal design by comparing the obtained optimal trajectory with the solution from existing trajectory design strategies. The simulation setups are initialized as:  $H = 10$  m,  $\frac{\beta P}{\sigma^2} = 80$  dB,  $D_0 = (0, 0)$  m,  $D_1 = (200, 40)$  m and  $D_2 = (0, 100)$  m.

At first, with a fixed angle  $\alpha = -0.047$ , the effect of absolute tension  $Q_0$  is depicted in Fig. 8(a). We observe that a larger  $Q_0$  makes the generated rope closer to  $D_0$ , while decreasing  $Q_0$  leads to an upward movement of the generated rope. This indicates a unique  $Q_0$  can be found resulting in

a generated rope passing through  $\mathbf{D}_2$ . From the figure, with our simulation setup, the optimal  $Q_0$  is clearly equal to 0.74 when  $\alpha = -0.047$ . The correctness of the proved Lemma 4 is therefore confirmed. Next, in Fig. 8(b), we show the effect of  $\alpha$  on the generated rope with a fixed  $\hat{Q}_0 = 40.461$ . Clearly, with different initial tension angle  $\alpha$ , the initial curve slope at  $\mathbf{D}_1$ , which is directly influenced by  $\alpha$ , becomes different. Besides, we can also observe that the generated rope becomes closer to  $\mathbf{D}_0$  when  $\alpha$  increases. The Lemma 5 of monotonic effect of angle  $\alpha$  is thus confirmed.

Then, with  $Q_0 = Q_0^*(\alpha)$  which guarantees the generated rope passing through  $\mathbf{D}_2$ , we study the behaviour of the generated rope with varying tension angle  $\alpha$  in Fig. 9. Clearly illustrated, when  $Q_0$  guarantees the rope passing through  $\mathbf{D}_2$ , the rope segment between  $\mathbf{D}_1$  and  $\mathbf{D}_2$  tends to be expanded towards the direction to  $\mathbf{D}_0$ . Note that the rope lengths of segment between  $\mathbf{D}_1$  and  $\mathbf{D}_2$  with different initial angle  $\alpha$  have been calculated and listed in the legend. By comparing the length of rope segment, we can find that the rope length  $S$  is monotonically increasing with respect to the initial tension angle  $\alpha$ . As a result, the conclusion in Lemma 6 is also confirmed. Therefore, via greedily searching, our design for insufficient rope mass  $m$ , i.e., insufficient time duration  $T$ , is capable of finding the optimal initial rope tension and resulting a global optimal UAV trajectory.

Furthermore, we validate the optimality of our design (i.e., **global optimal**) by comparing it with two existing efficient trajectory design strategies:

- **successive convex programming (SCP)-based design:** As a popular strategy, the SCP-based design quantizes the trajectory over time with a resolution  $\delta T$ . The value of  $\delta T$  is assumed to be sufficiently small, so that the UAV can be considered to be static in a time slot with length  $\delta T$ . Then by dividing the UAV trajectory into  $\frac{T}{\delta T}$  time slots and optimizing the UAV positions in all time slots via SCP techniques, a suboptimal UAV trajectory can be obtained. However, note that the SCP-based design can only obtain a discretized solution, which is required to be modified before realistic applications. Generally, the trajectory is modified by letting the UAV fly between discrete points with a uniform speed along a straight line. The speed is dependant on the distance between these discrete points and the time resolution. For an accurate comparison, we evaluate the corresponding performance based on the modified realistic trajectory.
- **successive-hover-fly (SHF)-based design:** In the SHF structure, the UAV will successively visit all hovering points and fly along a straight line with maximum speed  $V$  in each two neighbour hovering points. For comparison, we construct the SHF-based design in our problem (OP) with a single hovering point. The UAV flies from  $\mathbf{D}_1$  to a designed hovering point and back to  $\mathbf{D}_2$

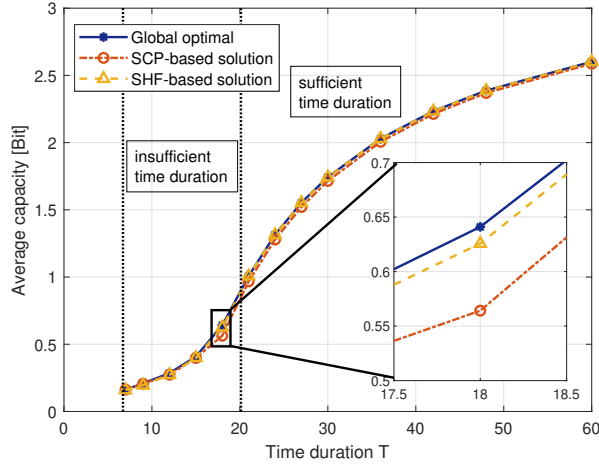


Fig. 10. Performance comparison with different time duration  $T$ .

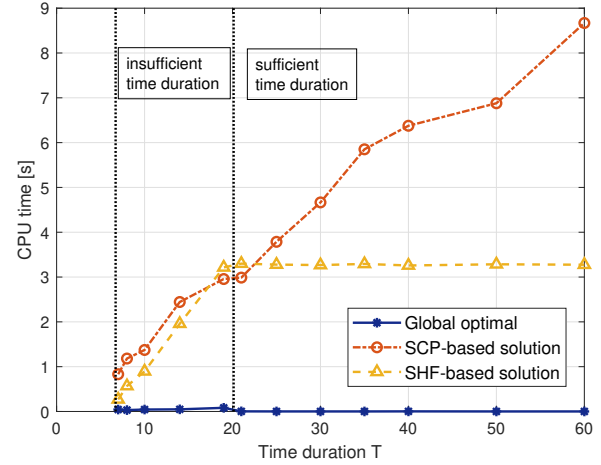


Fig. 11. Computational complexity comparison with different time duration  $T$ .

along straight lines with a hovering behaviour at the hovering point. In simulations, we find the defined hovering points and hovering duration via exhaustive search.

The default simulation setups for the comparison with existing strategies are as following:  $H = 10\text{m}$ ,  $\frac{\beta P}{\sigma^2} = 30\text{dB}$ ,  $\mathbf{D}_0 = (0, 0)\text{m}$ ,  $\mathbf{D}_1 = (100, 50)\text{m}$  and  $\mathbf{D}_2 = (40, 80)\text{m}$ , which can provide us a better view of the differences in trajectories designed by different strategies. We depict in Fig. 10 the average capacity obtained from all three strategies with varying time duration  $T$  and in Fig. 11 the corresponding computational CPU time for the complexity comparison. From Fig. 10, clearly, a larger time duration  $T$  results in a higher average capacity for all strategies, which confirms the benefits of allocating more time resource to the communication task. By comparing the network performance in the enlarged figure, we find that our proposed solution always outperforms the two benchmarks, which validates the optimality of our proposed solution. On the other hand, by observing Fig. 11, we observe that our proposed solution also shows an extremely lower complexity compared to the two benchmarks, especially when the time duration  $T$  is relatively larger. This is due to the fact that we have built a closed-form expression for the optimal trajectory. Note that the complexity of SHF-based solution results from the exhaustive search of the hovering points. With relatively smaller  $T$ , the feasible region of hovering points tends to be smaller and leads to a lower complexity.

Finally, in Fig. 12(a), we show the results of different designed UAV trajectory from different strategies. We observe that the discrete points from SCP-based design are located much closer to the global optimal solution, which results from our proposed design. However, the modification (straight lines between discrete points) on SCP-based design for forming a continuous trajectory still makes the solution deviate from the optimal one. As for SHF-based design, the difference

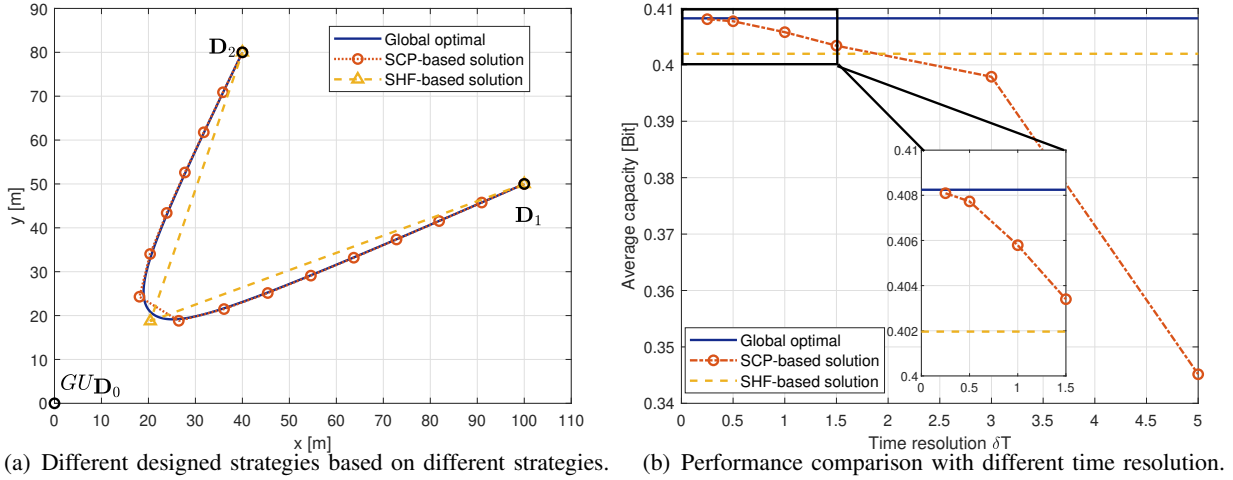


Fig. 12. Comparison of different strategies with  $T = 15s$ .

compared to the optimal solution obviously comes from the assumption of straight lines between hovering points, which is not optimal.

Then, we depict the average capacity of three designs, i.e.,  $\frac{U(\{x(t), y(t)\})}{BT}$ , in Fig. 12(b) for the system performance evaluation. Apparently, with higher time resolution (smaller  $\delta T$ ), the discretization errors in SCP-based design are reduced, so that a better average channel capacity, also a larger overall throughput, can be obtained. Although, the performance of SCP-based design is still upper bounded by that of our proposed solution, which further confirms the global optimality of our design. On the other hand, a higher resolution, a smaller  $\delta T$ , will also increase the number of variables to be optimized, which will lead to a higher complexity. By comparison, our proposed design is based on a closed-form expression which provides an absolutely lower complexity. Moreover, the SHF-based design is also below the optimal one and becomes even better than the result from SCP-based design with a lower time resolution.

**Remark.** Note that it should be mentioned that SCP-based design requires a convex approximation of the quantized problem, which is much likely inaccessible in a scenario with complex models. By contrast, the derivations in our proposed strategy for single-user network only requires a monotonic increasing property (Property 1) on APF, i.e., position closer to user has a better performance, which can be easily satisfied in most scenarios, like the scenario with probabilistic LoS model. Therefore, our proposed strategy is again demonstrated to have a high capability in extensions. In particular, for single-user networks, as long as the Property 1 holds for the corresponding APF, the global optimality of extended solution can also be guaranteed. For multi-user networks, this novel strategy can also enable the corresponding characterization and make the optimal solution analyzable.

## VII. CONCLUSION

In this paper, we proposed a novel strategy for optimally designing the UAV trajectory. We first introduce the mechanical concept of APF into trajectory design and consider a single-user network as an example network for strategy clarification. By representing the opposite of the objective in design with artificial potential energy, the trajectory design problem is reformulated to a mechanical problem, namely a shape design of a rope in equilibrium. In the considered network, the optimal rope shape is investigated via mechanical principles. Different approaches are provided for obtaining the optimal solution to the problems under different assumptions of rope mass. The optimal UAV trajectory is equivalently constructed from the optimal rope shape. The optimality of obtained solution is further confirmed by the simulation results. It is worthwhile to mention that a **close-form expression** of the globally optimal **curving** trajectory is for the first time provided, which is expected to open a door for researchers in this area handling similar/related problems.

As for potential extensions, by defining a different APF according to the objective, our proposed novel strategy can be directly extended into various UAV systems with obstacle avoidance, different channel and topology models, user numbers, design objectives, UAV tasks and so on, which confirms the high adaptability. More specifically, when the user has a continuously changing location, we can still model the user mobility into a conditionally varying APF and construct the equivalent physical problem. For the scenario where the acceleration limit is necessary to be considered, we can also model the limit as a constraint on the curvature and line density variation in the equivalent physical problem. By combining multiple APFs from different users into one integrated APF, the trajectory design problem in multi-user scenario also becomes possible to be analyzed in physics domain.

Moreover, it should be pointed out that in comparison to traditional trajectory design, the complexity of calculating the UAV trajectory based on the close-form expression is negligible. Hence, applying learning process (even the time-consuming deep reinforcement learning) on the UAV become highly possible, which could handle the UAV network serving dynamic GUs, where the number and locations of the users changes in a quasi-static manner. We finalize the work by stressing that via the introduced equivalence to mechanical problems, not only the mechanical principles, but also the physics simulation softwares, e.g., *Interactive physics* and *QuickField* which allow to self-define a force field, highly probably become efficient tools in the design of UAV trajectories.

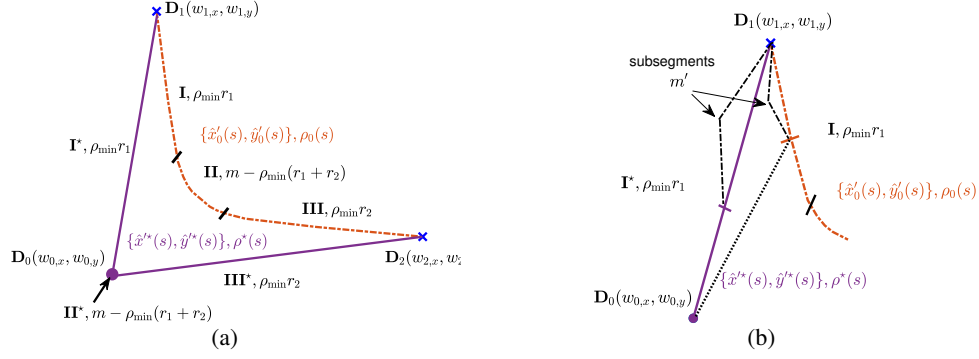


Fig. 13. Figures for Proof 1. (a) An example of optimal solution and a feasible solution with sufficient rope mass. (b) An example of subsegments in I and  $I^*$ .

## APPENDIX A

### PROOF OF LEMMA 1

In the rope defined by (21), (22) and (23), the total mass  $m$  is divided into three parts, i.e., mass  $\rho_{\min} r_1$  and  $\rho_{\min} r_2$  on two straight lines  $I^*$  and  $III^*$ , and a mass point  $II^*$  with mass  $m - \rho_{\min}(r_1 + r_2)$  at  $D_0$ , as marked in Fig. 13(a). For any feasible solution  $\{\hat{x}'_0(s), \hat{y}'_0(s)\}, \rho_0(s)$  and  $S_0$  to problem (P3), starting with  $D_1$ , we can accordingly cut it into three segments I, II and III, respectively with mass  $\rho_{\min} r_1$ ,  $m - \rho_{\min}(r_1 + r_2)$  and  $\rho_{\min} r_2$ . An example of cutting a feasible solution is shown in Fig. 13(a). Hence, the optimality of the solution can be shown by proving that the potential energy of each segment  $i \in \{I, II, III\}$  in the feasible solution is lower-bounded by that of corresponding segment  $i^*$ . According to the monotonic Property 1 of APF, the point  $D_0$  has the lowest potential in the whole field, i.e., the potential energy of segment  $II^*$  is definitely lower than or equal to the one of segment II. Hence, the remaining tasks are the proof for segment I and segment II.

Let us then consider segment I and denote by  $s_I$  the corresponding total length. In particular, for a subsegment in I which starts from  $D_1$  and has a length of  $s$ , we denote by  $U_I(s)$  and  $m_I(s)$  the potential energy and mass of this subsegment. An example of such subsegment is shown in Fig. 13(b). Hence, we have

$$U_I(s) = \int_0^s R''(\hat{x}'_0(s'), \hat{y}'_0(s')) \rho_0(s') ds', \quad m_I(s) = \int_0^s \rho_0(s') ds', \quad s \in [0, s_I]. \quad (70)$$

Immediately, we have the potential energy of segment I given by  $U_I(s_I)$  and  $m_I(s_I) = \rho_{\min} r_1$ .

Correspondingly, we can also define by  $s_{I^*}$ ,  $U_{I^*}(s)$  and  $m_{I^*}(s)$  the total length of for segment  $I^*$ , the potential energy and mass of a subsegment in segment  $I^*$ . According to the definition of potential energy and mass of the subsegment, we can formulate the following relations in differentiation

$$\frac{dU_I(s)}{dm_I(s)} = R''(\hat{x}'_0(s), \hat{y}'_0(s)), \quad \frac{dU_{I^*}(s)}{dm_{I^*}(s)} = R''(\hat{x}^*(s), \hat{y}^*(s)). \quad (71)$$

Note that for a given value of  $m_I(s) = m' \in [0, \rho_{\min} r_1]$ , the distance from the other end  $(\hat{x}'_0(s), \hat{y}'_0(s))$  of the subsegment in I to  $D_0$  is lower-bounded by  $\frac{\rho_{\min} r_1 - m'}{\rho_{\min}} = r_1 - \frac{m'}{\rho_{\min}}$ , while this lower-bound is

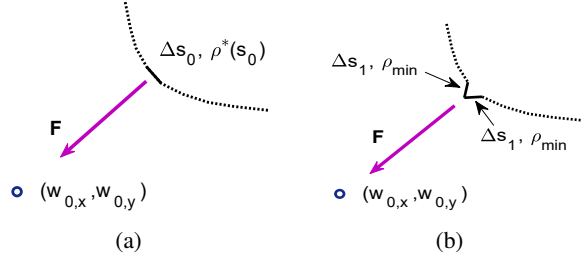


Fig. 14. For proof of density property. (a) An example for a sufficiently short segment. (b) Modification with lower potential energy. exactly the distance from the other end of the subsegment in  $I^*$  to  $D_0$  when  $m_{I^*}(s) = m'$ , as implied in Fig. 13(b). According to Property 1 which shows that APF  $R''(x, y)$  is monotonic increasing with respect to distance  $r(x, y)$ , we can conclude that when  $m_I(s) = m_{I^*}(s) = m' \in [0, \rho_{\min} r_1]$ ,  $\frac{dU_I(s)}{dm_I(s)}|_{m_I(s)=m'} \geq \frac{dU_{I^*}(s)}{dm_{I^*}(s)}|_{m_{I^*}(s)=m'}$  holds. As  $m_I(0) = m_{I^*}(0) = 0$ ,  $m_I(s_I) = m_{I^*}(s_{I^*}) = \rho_{\min} r_1$  and  $U_I(0) = U_{I^*}(0) = 0$  hold, we have  $U_I(s_I) \geq U_{I^*}(s_{I^*})$ , namely segment  $I^*$  possesses lower potential energy than segment I. Similarly, we have the potential energy of segment  $III^*$  is lower than that of segment III.

Thus, for any feasible solution to (P3), the corresponding potential energy is not lower than that of the solution defined by (21), (22) and (23), i.e., the optimality of the constructed solution is proven.

## APPENDIX B

### PROOF OF LEMMA 2

We prove the lemma by contradiction. Assume that in the optimal rope solution  $\{\hat{x}^*(s), \hat{y}^*(s)\}$ ,  $\rho^*(s)$  and  $S'^*$  of problem (P3),  $\exists s_0 \in [0, S'^*]$  such that  $(\hat{x}^*(s_0), \hat{y}^*(s_0)) \neq D_0 = (w_{0,x}, w_{0,y})$  and  $\rho^*(s_0) > \rho_{\min}$ . Then, we select a sufficiently short segment  $\Delta s_0$  around  $s_0$ , such that the line density in the segment  $\Delta s_0$  can be considered as a constant  $\rho^*(s_0)$ , as shown in Fig. 14(a). And we can construct two rope segments with line density  $\rho_{\min}$  and length  $\Delta s_1 = \frac{1}{2} \frac{\rho^*(s_0)}{\rho_{\min}} \Delta s_0$ . The total mass of the two introduced segments  $\Delta s_1$  is the same as that of segment  $\Delta s_0$ . Thus, by replacing  $\Delta s_0$  with two segments  $\Delta s_1$ , as shown in Fig. 14(b), the total mass of the rope is not affected. Clearly, we have  $2\Delta s_1 = \frac{\rho^*(s_0)}{\rho_{\min}} \Delta s_0 > \Delta s_0$ , which implies that the segment length  $2\Delta s_1$  is enough to connect the rope. Furthermore, as segments  $\Delta s_1$  are obviously closer to the point  $D_0$  than segment  $\Delta s_0$ , a reduction on the artificial potential energy is observed in the replacement behavior, according to the monotonic Property 1 of APF. Therefore, a rope solution with better objective for (P3) is constructed in Fig. 14(b), which is contradict to the assumption of the optimal rope solution.

## REFERENCES

- [1] L. Gupta, R. Jain and G. Vaszkun, "Survey of Important Issues in UAV Communication Networks," *IEEE Commun. Surv. & Tuts.*, vol. 18, no. 2, pp. 1123-1152, Secondquarter 2016.
- [2] T. Tomic, K. Schmid, P. Lutz, and et. al., "Toward A Fully Autonomous UAV: Research Platform for Indoor and Outdoor Urban Search and Rescue," *IEEE Rob. & Auto. Mag.*, vol. 19, no. 3, pp. 46-56, 2012.

- [3] N.H. Motlagh, M. Bagaa and T. Taleb, "UAV-Based IoT Platform: A Crowd Surveillance Use Case," *IEEE Commun. Mag.*, vol. 55, no. 2, pp. 128-134, 2017.
- [4] H. Hellou, O. Bekkouch, M. Bagaa and T. Taleb, "Aerial Control System for Spectrum Efficiency in UAV-to-Cellular Communications," *IEEE Commun. Mag.*, vol. 56, no. 10, pp. 108-113, 2018.
- [5] M. Cui, G. Zhang, Q. Wu and D.W.K. Ng, "Robust Trajectory and Transmit Power Design for Secure UAV Communications," *IEEE Trans. Veh. Technol.*, vol. 67, no. 9, pp. 9042-9046, 2018.
- [6] Y. Zeng, R. Zhang and T. J. Lim, "Wireless Communications with Unmanned Aerial Vehicles: Opportunities and Challenges," *IEEE Commun. Mag.*, vol. 54, no. 5, pp. 36-42, May 2016.
- [7] X. Zhang and L. Duan, "Optimization of Emergency UAV Deployment for Providing Wireless Coverage," *Globecom 2017*, Singapore, 2017, pp. 1-6.
- [8] J. Lyu, Y. Zeng, R. Zhang, and T. J. Lim, "Placement Optimization of UAV-Mounted Mobile Base Stations," *IEEE Commun. Lett.*, vol. 21, no. 3, pp. 604-607, Mar. 2017.
- [9] M. Alzenad, A. El-Keyi and H. Yanikomeroglu, "3-D Placement of an Unmanned Aerial Vehicle Base Station for Maximum Coverage of Users With Different QoS Requirements," *IEEE Wireless Commun. Lett.*, vol. 7, no. 1, pp. 38-41, Feb. 2018.
- [10] Y. Chen, W. Feng and G. Zheng, "Optimum Placement of UAV as Relays," *IEEE Commun. Lett.*, vol. 22, no. 2, pp. 248-251, 2017.
- [11] P. Li and J. Xu, "Fundamental Rate Limits of UAV-Enabled Multiple Access Channel with Trajectory Optimization," *IEEE Trans. Wireless Commun.*, vol. 19, no. 1, pp. 458-474, Jan. 2020.
- [12] Q. Wu, J. Xu, and R. Zhang, "Capacity Characterization of UAV-Enabled Two-User Broadcast Channel," *IEEE J. Sel. Areas Commun.*, vol. 36, no. 9, pp. 1955-1971, Sep. 2018.
- [13] Y. Zeng, R. Zhang and T. J. Lim, "Throughput Maximization for UAV-Enabled Mobile Relaying Systems," *IEEE Trans. Commun.*, vol. 64, no. 12, pp. 4983-4996, Dec. 2016.
- [14] Y. Zeng, J. Xu, and R. Zhang, "Energy Minimization for Wireless Communication with Rotary-Wing UAV," *IEEE Trans. Wireless Commun.*, vol. 18, no. 4, pp. 2329-2345, Apr. 2019.
- [15] C. Zhan and H. Lai, "Energy Minimization in Internet-of-Things System Based on Rotary-Wing UAV," in *IEEE Wireless Commun. Lett.*, vol. 8, no. 5, pp. 1341-1344, Oct. 2019.
- [16] Y. Zeng, and R. Zhang, "Energy-efficient UAV Communication with Trajectory Optimization," *IEEE Trans. Wireless Commun.*, vol. 16, no. 6, pp. 3747-3760, Jun. 2017.
- [17] C. Zhan, Y. Zeng and R. Zhang, "Energy-Efficient Data Collection in UAV Enabled Wireless Sensor Network," *IEEE Wireless Commun. Lett.*, vol. 7, no. 3, pp. 328-331, June 2018.
- [18] Y. Zeng, X. Xu and R. Zhang, "Trajectory Design for Completion Time Minimization in UAV-Enabled Multicasting," *IEEE Trans. Wireless Commun.*, vol. 17, no. 4, pp. 2233-2246, 2018.
- [19] Y. Hu, X. Yuan, J. Xu and A. Schmeink, "Optimal 1D Trajectory Design for UAV-Enabled Multiuser Wireless Power Transfer," *IEEE Trans. Commun.*, vol. 67, no. 8, pp. 5674-5688, Aug. 2019.
- [20] M.E. Gurtin, "An Introduction to Continuum Mechanics," *Academic press*, 1982.
- [21] M.G. Park, J.H. Jeon and M.C. Lee, "Obstacle Avoidance for Mobile Robots Using Artificial Potential Field Approach with Simulated Annealing," *2001 IEEE ISIE Proceedings*, Vol. 3, 2001.
- [22] Y. Chen, G. Luo, Y. Mei, J. Yu and X. Su, "UAV Path Planning Using Artificial Potential Field Method Updated by Optimal Control Theory," *Int. J. Syst. Sci.*, vol. 47, no. 6, pp. 1407-1420, 2016.
- [23] F. Cheng, S. Zhang, Z. Li, Y. Chen, N. Zhao, F.R. Yu, and V.C.M. Leung, "UAV Trajectory Optimization for Data Offloading at the Edge of Multiple Cells," *IEEE Trans. Veh. Technol.*, vol. 67, no. 7, pp. 6732-6736, July 2018.
- [24] L. Xie, J. Xu, and R. Zhang, "Throughput Maximization for UAV-Enabled Wireless Powered Communication Networks," *IEEE Internet Things J.*, vol. 6, no. 2, pp. 1690-1703, Apr. 2019.
- [25] J. Xu, Y. Zeng, and R. Zhang, "UAV-Enabled Wireless Power Transfer: Trajectory Design and Energy Optimization," *IEEE Trans. Wireless Commun.*, vol. 17, no. 8, pp. 5092-5106, Aug. 2018.
- [26] S. Pradhan and S. Sinha, "Analytical Statics", *Academic Publishers*, 2006.
- [27] V.F. Zaitsev and A.D. Polyanin, "Handbook of exact solutions for ordinary differential equations," *CRC press*, 2002.



- [28] T. Bonnesen and W. Fenchel, “Theory of convex bodies,” *Moscow: BCS Associates*, 1987.